The Astrophysical Journal Supplement Series, 259:43 (24pp), 2022 April https://doi.org/10.3847/1538-4365/ac45f7

Virgo Filaments. II. Catalog and First Results on the Effect of Filaments on Galaxy Properties

Gianluca Castignani[1,2,3], Benedetta Vulcani[4], Rose A. Finn[5], Francoise Combes[6], Pascale Jablonka[3,7], Gregory Rudnick[8], Dennis Zaritsky[9], Kelly Whalen[10], Kim Conger[8], Gabriella De Lucia[11], Vandana Desai[12], Rebecca A. Koopmann[13], John Moustakas[5], Dara J. Norman[14], and Mindy Townsend[8]
[1] Dipartimento di Fisica e Astronomia, Alma Mater Studiorum Università di Bologna, Via Gobetti 93/2, I-40129 Bologna, Italy; gianluca.castignani@unibo.it
[2] INAF—Osservatorio di Astrofisica e Scienza dello Spazio di Bologna, via Gobetti 93/3, I-40129, Bologna, Italy
[3] Institute of Physics, Laboratory of Astrophysics, Ecole Polytechnique Fédérale de Lausanne (EPFL), Observatoire de Sauverny, CH-1290 Versoix, Switzerland
[4] INAF—Osservatorio astronomico di Padova, Vicolo Osservatorio 5, I-35122 Padova, Italy
[5] Department of Physics and Astronomy, Siena College, 515 Loudon Road, Loudonville, NY 12211, USA
[6] Observatoire de Paris, LERMA, Collège de France, CNRS, PSL University, Sorbonne University, F-75014, Paris, France
[7] GEPI, Observatoire de Paris, Université PSL, CNRS, Place Jules Janssen, F-92190 Meudon, France
[8] University of Kansas, Department of Physics and Astronomy, 1251 Wescoe Hall Drive, Room 1082, Lawrence, KS 66049, USA
[9] Steward Observatory, University of Arizona, 933 North Cherry Avenue, Tucson, AZ 85721-0065, USA
[10] Department of Physics & Astronomy, Dartmouth College, 6127 Wilder Laboratory, Hanover, NH 03755, USA
[11] INAF—Astronomical Observatory of Trieste, via G.B. Tiepolo 11, I-34143 Trieste, Italy
[12] Spitzer Science Center, California Institute of Technology, MS 220-6, Pasadena, CA 91125, USA
[13] Department of Physics & Astronomy, Union College, Schenectady, NY, 12308, USA
[14] National Optical Astronomy Observatory, 950 North Cherry Avenue, Tucson, AZ 85750, USA
Received 2021 June 15; revised 2021 October 8; accepted 2021 October 20; published 2022 March 23

Abstract

Virgo is the nearest galaxy cluster; it is thus ideal for studies of galaxy evolution in dense environments in the local universe. It is embedded in a complex filamentary network of galaxies and groups, which represents the skeleton of the large-scale Laniakea supercluster. Here we assemble a comprehensive catalog of galaxies extending up to ∼12 virial radii in projection from Virgo to revisit the cosmic-web structure around it. This work is the foundation of a series of papers that will investigate the multiwavelength properties of galaxies in the cosmic web around Virgo. We match spectroscopically confirmed sources from several databases and surveys including HyperLeda, NASA Sloan Atlas, NASA/IPAC Extragalactic Database, and ALFALFA. The sample consists of ∼7000 galaxies. By exploiting a tomographic approach, we identify 13 filaments, spanning several megaparsecs in length. Long $>17\,h^{-1}$ Mpc filaments, tend to be thin ($<1\,h^{-1}$ Mpc in radius) and with a low-density contrast (<5), while shorter filaments show a larger scatter in their structural properties. Overall, we find that filaments are a transitioning environment between the field and cluster in terms of local densities, galaxy morphologies, and fraction of barred galaxies. Denser filaments have a higher fraction of early-type galaxies, suggesting that the morphology–density relation is already in place in the filaments, before galaxies fall into the cluster itself. We release the full catalog of galaxies around Virgo and their associated properties.

Unified Astronomy Thesaurus concepts: Galaxy clusters (584); Virgo Cluster (1772); Large-scale structure of the universe (902); Astronomy databases (83); Catalogs (205); Surveys (1671)

Supporting material: interactive figure, machine-readable tables

1. Introduction

Galaxies in the universe are not distributed uniformly at the megaparsec scales. Large galaxy redshift surveys have revealed that the universe has a prominent weblike structure made by dense clusters and groups, elongated filaments, planar sheets, and voids, called the cosmic web (Tifft & Gregory 1976; Joeveer et al. 1978; Bond et al. 1995). Galaxies are continuously funneled into higher-density cluster environments through filaments, which host ∼40% of the galaxies (e.g., Jasche et al. 2010; Tempel et al. 2014; Cautun et al. 2014). Therefore, the analysis of filamentary structures can carry insights into the assembly history of large-scale structures.

Characterizing the cosmic web and flow of galaxies in the nearby universe is not an easy task, and many strategies have been proposed, based on either observations (Tully et al. 2013, 2016) or simulations (e.g., Libeskind et al. 2018, 2020). These methods often rely on the study of the geometry of the galaxy density field or of the tidal field to reconstruct the cosmic web, which indeed consists of a set of structures that are anisotropic in shape (e.g., elongated filaments), multiscale (groups, clusters, and filaments that can extend from a few to 100 Mpc), and are intricately connected (see, e.g., Cautun et al. 2014). The absence of both a common definition for the cosmic filaments and a unique operative procedure to identify the filamentary structures, as well as the lack of fields observed with a very high sampling rate, have been major obstacles in investigating not only the structure of the cosmic web but also its impact on galaxy evolution.

Despite difficulties, filamentary structures of the cosmic web have been identified in both simulations (e.g., Aragon-Calvo et al. 2008; Cautun et al. 2014; Chen et al. 2015; Laigle et al. 2018; Kraljic et al. 2019; Kuchner et al. 2020, 2021; Rost et al. 2021) and galaxy surveys (e.g., Tempel et al. 2014; Alpaslan

et al. 2014; Chen et al. 2016; Laigle et al. 2018; Kraljic et al. 2018; Malavasi et al. 2017, 2020a, 2020b). Many works have also suggested that filaments affect the evolution of the integrated properties of galaxies (e.g., Geach et al. 2011; Koyama et al. 2011; Sobral et al. 2011; Mahajan et al. 2012; Pintos-Castro et al. 2013; Tempel & Libeskind 2013a; Tempel et al. 2013; Zhang et al. 2013; Koyama et al. 2014; Santos et al. 2014; Malavasi et al. 2017; Mahajan et al. 2018) and the distribution of satellites around galaxies (Guo et al. 2014), at any redshift, but results are still controversial. Overall, filament galaxies tend to be more massive, redder, more gas poor, and have earlier morphologies than galaxies in voids (Rojas et al. 2004; Hoyle et al. 2005; Kreckel et al. 2011; Beygu et al. 2017; Kuutma et al. 2017). Some studies have also reported an increased fraction of star-forming galaxies (Porter & Raychaudhury 2006; Fadda et al. 2008; Porter et al. 2008; Biviano et al. 2011; Mahajan et al. 2012; Darvish et al. 2014) and higher metallicities and lower electron densities (Darvish et al. 2015) in filaments with respect to field environments.

Other studies even found evidence of a distinct impact of filaments on galaxy properties and different gas phases. Vulcani et al. (2019) showed that ionized Hα clouds in some filament galaxies extend far beyond what is seen for other noncluster galaxies. The authors suggest this may be due to the effective cooling of the dense star-forming regions in filament galaxies, which ultimately increases the spatial extent of the Hα emission. Even atomic H I gas reservoirs are impacted by the filament environments (Kleiner et al. 2017; Odekon et al. 2018; Blue Bird et al. 2020; Lee et al. 2021). The global properties of galaxies' gas reservoirs as a function of distance to the filament and local density are still debated. Some studies claimed that galaxy and halo properties (e.g., luminosities, masses, accretion rate, concentration) depend mostly on local density, while the filament environment has no additional effects beyond the ones related to the local density enhancement (Yan et al. 2013; Eardley et al. 2015; Brouwer et al. 2016; Goh et al. 2018).

Further investigations are therefore clearly needed. Our approach is to focus on the area around Virgo, the benchmark cluster in the local universe. It is embedded in a complex filamentary network as it indeed belongs to the Laniakea supercluster (Tully et al. 2014). The closeness of Virgo and its associated high spectroscopic completeness makes its field ideal for studies of galaxy evolution over a large range in environments.

Numerous studies have characterized the galaxy population of the Virgo cluster (Kim et al. 2014) and evaluated the associated atomic and molecular gas content (Giovanelli et al. 2005; Chung et al. 2009; Boselli et al. 2014a, 2014b, 2014c), dust (Davies et al. 2010) stellar masses (Ferrarese et al. 2012), and star formation (Boselli et al. 2014d). However, galaxies in the surrounding regions have received relatively little attention. Tully (1982) identified prolate and oblate overdensities of galaxies connected to the cluster. Nonetheless, due to the limited size of their sample, these elongated structures were not clearly revealed as conventional narrow filaments. A better characterization of these structures requires improved statistics from larger galaxy samples, particularly those with fainter galaxies. Building upon Tully's results, Kim et al. (2016) used the seventh release of the Sloan Digital Sky Survey (SDSS; Abazajian 2008) combined with the HyperLeda catalog (Makarov et al. 2014) to more firmly identify the filamentary structures within an extensive volume around the Virgo cluster. While providing a detailed characterization of the filaments around the Virgo cluster, Kim et al. (2016) did not release their environmental classification.

In Castignani et al. (2022, from now on Paper I) we therefore assemble an independent catalog of Virgo and the surrounding volume. We accomplish this by matching and vetting several existing catalogs, with the intent of releasing a comprehensive catalog of galaxies in the filaments around Virgo, extending out to $\sim$12 virial radii in projection (i.e., $\sim$24 Mpc) from the cluster, with a small fraction (7%) of galaxies reaching even higher distances, up $\sim$40 Mpc from Virgo. Two strengths of this catalog are that (1) we have high completeness because we merge sources from multiple catalogs of local galaxies, and (2) we have low contamination because we visually inspect every source in our sample.

Here we describe more in detail our adopted procedure and release the catalog (see the Appendix). With respect to Paper I, we refine both the source catalog by visually inspecting each object to remove duplicates, stars, and "shredded" galaxies and by excluding galaxies in the southern hemisphere where SDSS has poor spectroscopic coverage and filament definition (see Section 3.3).

Overall, we consider a larger survey area in the northern hemisphere than that covered by Kim et al. (2016). This allows us to identify and characterize additional filamentary structures to the north and east of the Virgo cluster that were not identified by Kim et al. (2016).

This catalog forms the foundation of a series of papers aimed at investigating the effect of the filament environment on processing the gas of galaxies and on global properties such as star formation and stellar content. The first exploration of the catalog has been presented in Paper I where we analyzed spatially integrated CO and H I observations for a subset of filament galaxies. We found a clear progression as one moves from field to filament and cluster in that galaxies in denser environments have a lower star formation rate, a higher fraction of galaxies in the quenching phase, an increasing proportion of early-type galaxies, and decreasing gas content. In addition, galaxies in the densest regions in filaments tend to be deficient in their molecular gas reservoirs, which fuel star formation. These results suggested that processes that lead to star formation quenching are already at play in filaments. Following this study, we are carrying out follow-ups at different wavelengths, with the aim of linking the galaxy stellar properties to the galaxy gas content. In particular, we will investigate the physical mechanisms responsible for the preprocessing using ongoing high-resolution observations in both CO and H I. In parallel, for a few hundred filament galaxies, we are conducting a Hα imaging survey to map the spatial distribution of the hot gas and to derive integrated star formation rates. All of these campaigns will be described in forthcoming papers.

The outline of this paper is the following. In Section 2 we describe how we build the catalog of galaxies around Virgo. In Sections 3 and 4 we characterize the cosmic-web environment around Virgo. In Section 5 we contrast the different parameterizations of the environment and in Section 6 we investigate the interplay between galaxy properties and their cosmic-web environment and describe our results. In Section 7 we draw our conclusions and summarize the paper.

Throughout this paper, we assume a Hubble constant of $H_0 = 100\,h\,\mathrm{km\,s^{-1}\,Mpc^{-1}}$, where $h = 0.74$ (e.g., Tully et al. 2008; Riess et al. 2019). Magnitudes are reported in the AB system.

2. The Spectroscopic Parent Catalog

To assemble a spectroscopic sample of galaxies around Virgo (R. A. = 187.°70, decl. = 12.°34, J2000), we start by creating a catalog from the union of HyperLeda (Makarov et al. 2014),[15] the NASA Sloan Atlas[16] (NSA; Blanton et al. 2011), and the ALFALFA α100 sample (Haynes et al. 2018) in the region covered by $100° < \mathrm{R.A.} < 280°$, $-1.°3 < \mathrm{decl.} < 75°$, and recession velocities $500 < v_r < 3300$ km s^{-1}. The southern limit coincides with the southern limit of the SDSS spectroscopic survey. We adopt this cut because we want high spectroscopic sampling to robustly identify and characterize filaments. However, this choice is different from what was done by Kim et al. (2016), who also characterized Virgo filaments to the south. The lower velocity cut is dictated by the need to avoid stars and galactic contamination. The higher velocity cut is set by the need to include all filaments, which are mostly located farther than Virgo ($cz \sim 1000$ km s^{-1}; Mei et al. 2007).

To build the sample, we start with all sources from HyperLeda that are classified as galaxies. We then match the HyperLeda sources to version 1 of the NSA, using a search radius of 10″ and a maximum velocity offset of 300 km s^{-1}. This updated version of the NSA extends to larger distances and contains additional fitted parameters[17] relative to version 0 presented in Blanton et al. (2011).

We initially allow for the same NSA source to be matched to multiple HyperLeda sources, and we later eliminate these duplicates by visual inspection (see below). We then append as new catalog entries any additional NSA sources that were not matched to HyperLeda. We repeat a similar match to version 0 of the NSA (Blanton et al. 2011) because some of the sources and redshifts differ between the two versions of the NSA catalogs. Versions 0 and 1 of NSA are complementary in terms of the number of galaxies that fall in the region of interest, which motivates the choice of querying both catalogs.

We then match the list of HyperLeda+NSA galaxies to the ALFALFA α100 sample (Haynes et al. 2018), limited to ALFALFA galaxies with $500 < v_r < 3300$ km s^{-1}. The northern limit of the ALFALFA survey is decl. = 36°, so we do not have ALFALFA coverage for our full survey area. However, 54% of our decl. < 36° sources are matched to an ALFALFA source, and this provides a rich sample for future studies on how the atomic gas reservoir is affected by the filament environments. As a blind H I survey, ALFALFA detects a higher fraction of low-mass star-forming galaxies relative to optical surveys (e.g., Durbala et al. 2020). However, at the relatively close distance of Virgo, we find only nine ALFALFA sources that are not already in either the Hyperleda or NSA catalogs. We add these nine sources to our catalog.

We assign a position (R.A., decl.) to each galaxy based on information in the source catalogs. We assign HyperLeda coordinates if they are available. If HyperLeda is not available, we then use NSA version 0, followed by NSA version 1, and ALFALFA. We assign recession velocities by the same process.

Next, we add to the sample 110 galaxies that have redshift-independent distances in the NASA/IPAC Extragalactic Database compendium of distances based on primary and secondary indicators (NED-D; Steer et al. 2017). These 110 galaxies have redshift-independent distances that correspond to cosmological velocities in the range of 500–3300 km s^{-1}, but they are missing in our catalog as their observed recession velocities are less than <500 km s^{-1}. Some of these sources are Virgo cluster members that are located near the caustics and thus have the largest deviation in velocity with respect to that of Virgo.

Finally, to compile as clean a sample as possible in the area of interest, we visually review each galaxy in our catalog to remove shredded galaxies, duplicates, and spurious objects. We also flag galaxies with nearby stars that might affect the photometry, and we recenter the coordinates of some galaxies, as needed.

To identify any remaining stars, we cross-match with the star catalog used by the Legacy Survey.[18] This catalog is built from Tycho-2 (MAG $_{\mathrm{VT}} < 13$) and Gaia-DR2 sources (G < 16). We look for matches within $r < 10''$ of our sources, and we find an additional two stars, which we remove.

While we require all of the sources to have a galaxy classification, we find that a number of HyperLeda sources are instead globular clusters in nearby galaxies, as identified by Ko et al. (2017). We therefore remove all sources with the prefix "S" in the Ko et al. (2017) catalog. On the basis of our cleaning procedure mainly aimed at removing duplicates and shredded objects, we found that ∼4% of HyperLeda sources in our region of interest are misclassified as galaxies.

For each galaxy, we also query the NED server to get its official NED name. We use the object name from HyperLeda as input if it is available. If not, we then use the NSA name and the ALFALFA/AGC name. If NED does not return a match by name for any of the catalog names, we then match the source by position, using a search radius of 10″. We include the input name used in the NED search as well as the official NED name in our table. Note that for some galaxies, we are not able to find a corresponding NED name.

Our final sample contains 6780 galaxies. The contributions from the different input catalogs are broken down in Table 1. The NSA v1 (v0) catalog provides 157 (122) galaxies that are not in the v0 (v1) version of the catalog. We stress that only nine galaxies are in the ALFALFA α100 sample, but not in the union of the HyperLeda and NSA source samples.

Table 1
Statistics of the Parent Sample

Catalog	No. of Galaxies	Fraction
Final	6780	1
HL	6622	0.98
NSA v1	5280	0.78
NSA v0	5245	0.77
α100	2336	0.34
NED-D	1959	0.29

[15] http://leda.univ-lyon1.fr/
[16] http://nsatlas.org
[17] https://www.sdss.org/dr13/manga/manga-target-selection/nsa/
[18] https://portal.nersc.gov/cfs/cosmo/data/legacysurvey/dr9/masking/gaia-mask-dr9.fits.gz

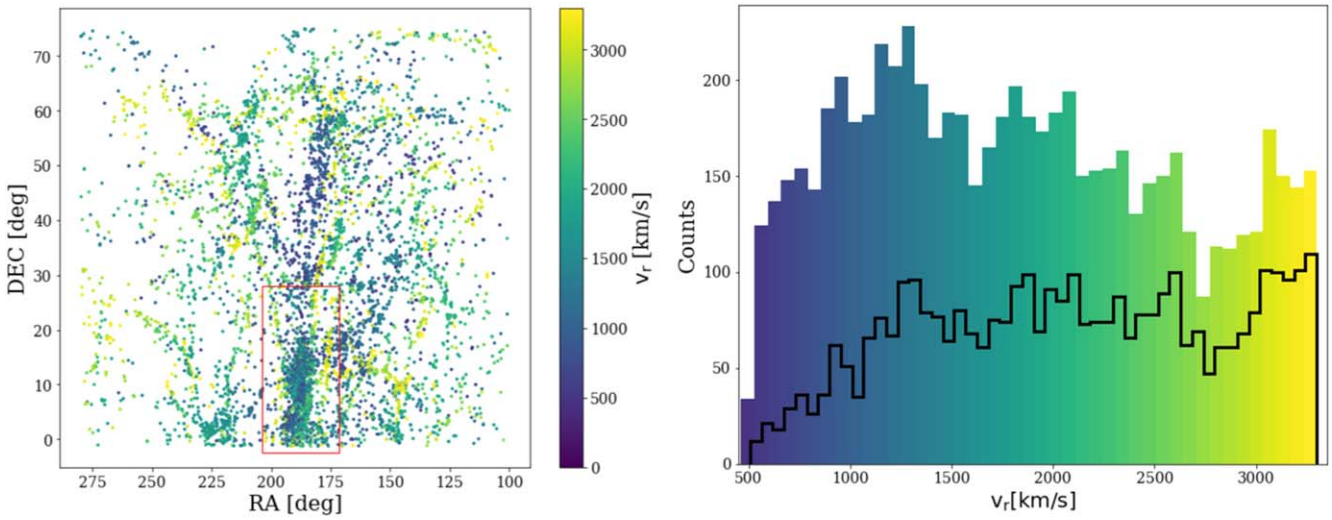

Figure 1. Left: spatial distribution of galaxies around the Virgo galaxy cluster, up to ∼12 virial radii from its center, in projection. Points show galaxies coded according to their recession velocities. The red rectangle shows the region of the Virgo cluster, which is examined in more detail in Figure 3. Right: radial velocity distribution of all galaxies in our catalog. The black solid line shows the distribution of galaxies brighter than the absolute magnitude completeness limit of the catalog ($M_r = -15.7$).

2.1. Photometry

We cross-match our catalog to the ninth public data release of the DESI Legacy Imaging Surveys (DR9; Dey et al. 2019), using a search radius of 10″. The Legacy Survey covers 14,000 deg^2 of extragalactic sky visible from the northern hemisphere in three optical bands (*g, r, z*) and four infrared bands. In this paper, we utilize only the *r*-band photometry from the DR9 catalogs to apply a magnitude cut and analyze galaxy properties in an absolute-magnitude-complete sample.

The available DR9 photometric catalogs are based on the Tractor fitting (Lang et al. 2016); like all automated photometry codes, Tractor struggles with providing meaningful models to clumpy, well-resolved galaxies. We therefore have efforts underway to measure custom photometry from the Legacy imaging that is optimized for large, nearby galaxies. In a forthcoming paper, we will present the multiband photometry for our entire catalog of sources in the field of Virgo, with a careful treatment of the extended galaxies (>0.′5 in size).

As most of the spectroscopic redshifts for galaxies in the catalog come from the SDSS, we adopt the SDSS completeness limit of $r = 17.77$. This corresponds to an absolute limit of $M_r = -15.7$ at a distance modulus of 33.5, approximately the upper limit of the survey.

2.2. The Final Catalog

To summarize, we have assembled a catalog of galaxies with $500 < v_r < 3300$ km s^{-1} located in the region surrounding the Virgo cluster (up to ∼12 virial radii, i.e., 24 Mpc, in projection from the center of Virgo) by combining the sources present in HyperLeda, NSA (v0 and v1), ALFALFA, and NED-D. This catalog is cleaned from spurious sources, stars, and duplicates and represents a unique starting point to define the cosmic web around the Virgo cluster, as detailed in what follows.

The final catalog (Table 1) contains 6780 galaxies, 3528 of which are above the absolute magnitude limit $M_r = -15.7$ ($\simeq M_r^\star + 3$, Blanton et al. 2005). The subsample of galaxies with $M_r < -15.7$ corresponds to a volume-limited sample, with the M_r limit corresponding to the SDSS $m_r = 17.77$ spectroscopic completeness limit at the maximum distance of the galaxies in our catalog. As we will describe in Section 3.3, we define different volume-limited subsamples appropriate for the distance range of each filament.

Figure 1 shows the projected spatial distribution of the final sample, color-coded by recession velocity (left panel), and the distribution of the recession velocity (right panel) for both the entire sample and subsample above the absolute magnitude limit.

Hereafter, to identify galaxies in different global environments (Sections 3 and 4.1), we will make use of the full catalog of ∼7000 galaxies. When we compute local densities to characterize the properties of galaxies in the different environments (from Section 4.2 onward), we will adopt the magnitude-complete sample.

3. The Virgo Cluster and Its Infalling Filaments

In this section we provide a characterization of the cosmic web around Virgo using the catalog of galaxies assembled above. We will rely on a widely used description of the cosmic flow around Virgo (Mould et al. 2000) and on redshift-independent distances, when available (Steer et al. 2017).

To properly investigate the effect of the megaparsec-scale environment on galaxy properties, it is necessary to provide both local and more global parameterizations of the density as, depending on the scale probed, different physical processes might shape galaxy properties. For example, the frequency of galaxy–galaxy interactions depends on the local density of galaxies, whereas gas accretion onto galaxies varies depending on whether the galaxy is a central or satellite galaxy in the parent halo mass. After computing the distances for all galaxies (Section 3.1), we will thus assign to all galaxies a global environment depending on whether they are in the Virgo cluster (Section 3.2) or in filamentary structures (Section 3.3). In Section 4.1 we will further investigate the presence of groups within filaments and assemble a sample of pure field galaxies, aided by the Kourkchi & Tully 2017 group catalog. We will finally evaluate local densities for all galaxies (Section 4.2), regardless of all of the above memberships.

We will then use these characterizations to (i) determine the filament profiles (Section 3.3.2), (ii) compare the different definitions of environment (Section 5), and (iii) describe the dependence of galaxy properties on the different environments (Section 6).

3.1. Cosmic Distances

To characterize the positions of all galaxies around Virgo, we convert heliocentric velocities v_r to intrinsic distances of the sources, according to the following steps.

First, we match our sample using the NED name to the NED-D catalog (Steer et al. 2017). The search yields a match for 1959 sources—corresponding to 29% of the total sample—and for these sources in what follows we will adopt the Steer et al. (2017) distances ($D_{z-\mathrm{independent}}$) as the final cosmic distances. We calibrate all $D_{z-\mathrm{independent}}$ assuming $H_0 = 74\,\mathrm{km\,s^{-1}\,Mpc^{-1}}$ used in this work. In the cases where the Steer et al. (2017) catalog provides multiple estimates for a given source, we adopt the median distance.

Second, we compute intrinsic distances following Mould et al. (2000), using their method for correcting observed recession velocities for peculiar motions associated with various attractors in the local universe. We derive the correction v_{LG} of the observed heliocentric velocity of our galaxies to the centroid of the Local Group (LG), as in Equation (A1) from Mould et al. (2000). Then we estimate the correction $v_{\mathrm{in,Virgo}}$ that takes into account the infall toward the Virgo attractor as in Equation (1) by Mould et al. (2000). Distances and radial velocities relative to the Virgo center are calculated by means of the cosine theorem (e.g., Karachentsev & Nasonova 2010). A cosmic velocity of $\sim$1016 km s^{-1} is assumed for Virgo, as found in NED. It is obtained by correcting Virgo heliocentric velocity to the LG centroid for our infall velocity and for the infall of Virgo into the Great Attractor, as described in Appendix A of Mould et al. (2000). We also assume a Virgo density profile $\rho(r) \propto r^{-2}$ and an amplitude $v_{\mathrm{fid}} = 200$ km s^{-1} for the Virgo infall velocity (Mould et al. 2000). Model-corrected velocities v_{model} are then derived as follows:

$$v_{\mathrm{model}} = v_r + v_{\mathrm{LG}} + v_{\mathrm{in,Virgo}}. \quad (1)$$

Here we ignore higher-order corrections in Equation (A2) by Mould et al. (2000) that are due to the infall of our galaxies toward the Great Attractor and Shapley supercluster. We also assume a linear dependence between velocities and distances.

Figure 2 shows the comparison between the model-corrected distances (D_{model}) and $D_{z-\mathrm{independent}}$ for galaxies with both redshift-independent and model-corrected distances. The median logarithmic difference is $\log(D_{\mathrm{model}}/D_{z-\mathrm{independent}}) = -0.03^{+0.12}_{-0.18}$. Here the reported uncertainties correspond to the 1σ confidence interval. The comparison yields a negligible bias and an rms scatter of $\sim$0.1 dex, which is consistent with that found in recent studies of the local universe (Leroy et al. 2019). The small differences, well within the uncertainties, between these values and those reported in Paper I are due to the different southern limits adopted in the two works, as here we do not consider galaxies at negative declinations as Paper I did. Although we find an overall agreement between redshift-independent and model-corrected distances, we do see an increased dispersion in the data points in Figure 2 along the y-axis at $\sim$17 Mpc, which corresponds to the distance of Virgo (Mei et al. 2007). The model correction for Virgo galaxies is more uncertain because peculiar velocities become significant as we approach the Virgo cluster.

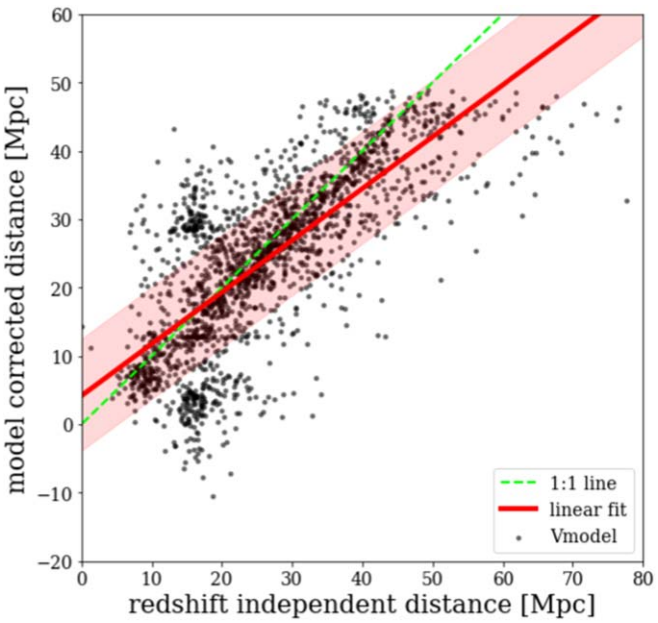

Figure 2. Comparison between the redshift-independent distances obtained from Steer et al. (2017) and those inferred from v_{model} for the galaxies present in the Steer et al. (2017) catalog (black points). The green line is the 1:1 relation. The red line shows the linear fit to the point, while the shaded red region denotes the corresponding $\pm 1\sigma$ scatter.

Overall, from the comparison presented in Figure 2 we conclude that for most of the galaxies in our sample with no redshift-independent distance, the model-corrected version is reliable enough to determine galaxy 3D positions and local density estimates (see Section 4.2). The model-corrected distances might not be as reliable for the Virgo cluster members, and in principle, this could impact our estimates of local density. Nonetheless, we will show in Section 6 that these uncertainties will not significantly affect our results.

To summarize, our adopted cosmic distances and velocities, D_{cosmic} and v_{cosmic}, are the redshift-independent distances and velocities, when available, and those derived as in Equation (1) for the remaining sources.

We then make use of the super-Galactic (SG) coordinate system, which was developed by Gérard de Vaucouleurs. This coordinate frame has the equator aligned with the SG plane, which consists of a planar distribution of nearby galaxy clusters. The SG system is thus ideal for studies of the cosmic web in the local universe. Therefore, assuming a linear relationship between v_{cosmic} and distance, galaxies have been mapped into the Cartesian SG frame. In this frame galaxy positions are defined in terms of their SG coordinates SGX, SGY, and SGZ (Tully et al. 2008). We note that the Virgo cluster center has (SGX; SGY; SGZ) = (−2.26; 9.90; −0.42) h^{-1} Mpc in the SG coordinate frame. At the coordinates of Virgo the SGY direction approximately corresponds to the line of sight.

3.2. Membership of the Virgo Cluster

To identify galaxies belonging to the Virgo cluster, we select galaxies within 3.6 h^{-1} Mpc from the Virgo cluster center in the 3D SG coordinate frame. The chosen radius corresponds approximately to $\sim 3r_{200}$, with $r_{200} = 1.09$ h^{-1} Mpc

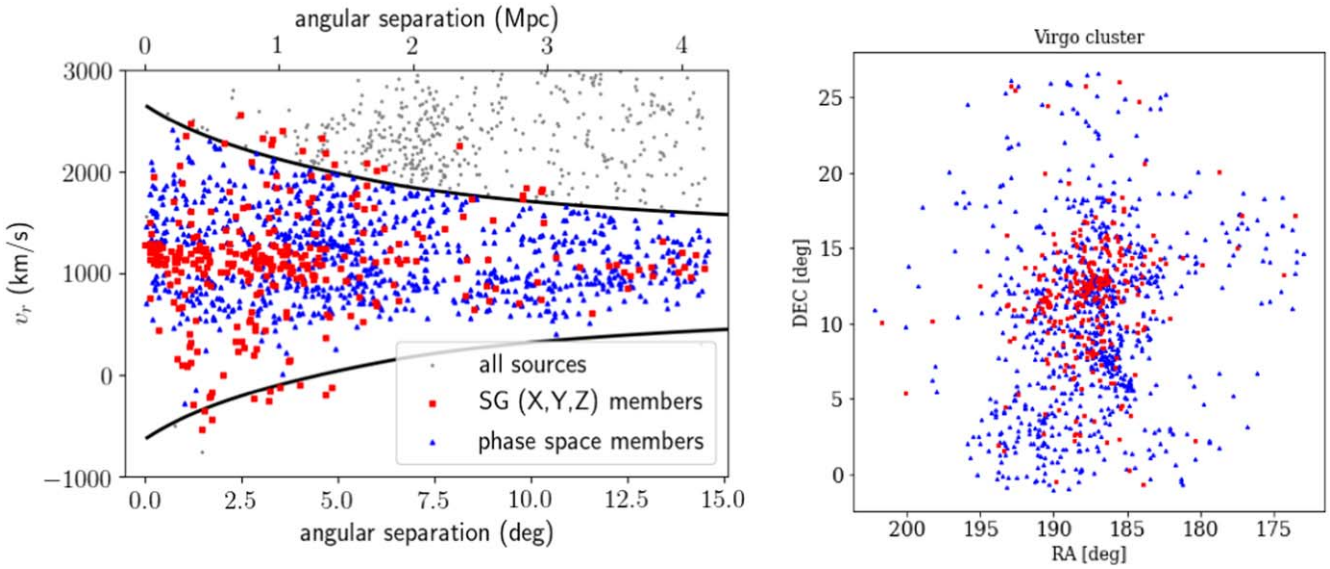

Figure 3. Left: phase-space diagram for sources in the field of the Virgo cluster. The solid lines show the radial dependence of the escape velocity in the phase-space diagram, according to the prescription by Jaffé et al. (2015). Cluster members defined in the super-Galactic (X, Y, Z) coordinate frame (red points) or within the region (blue points) delimited by the caustics (i.e., the two solid lines) are distinguished from the remaining sources in the field of Virgo cluster (gray points). Right: projected distribution of the cluster members on the sky.

(McLaughlin 1999) the radius that encloses 200 times the critical matter density. The position of the 311 Virgo members selected in this way in the phase-space diagram is shown in Figure 3. Overall, they fall within the region delimited by the caustics that are defined following the prescription by Jaffé et al. (2015), assuming the r_{200} radius and a concentration parameter of 2.8 as reported by McLaughlin (1999). As the adopted definition is rather conservative, we also consider as cluster members those galaxies that fall within the cluster region delimited in the phase-space diagram by the caustics, regardless of their position in the SG coordinates. The final cluster member sample is the union of the members defined in SG coordinates and those defined using the phase space, for a total of 1152 galaxies (526 above the magnitude completeness limit).

3.3. Filamentary Structures

Moving beyond the cluster, we aim to characterize its surrounding cosmic web in 3D. We start by considering the eight filamentary structures presented in Tully (1982), Kim et al. (2016): the W–M Sheet located to the south of Virgo; the nearby Ursa Major cloud in the North; the Virgo III filament to the south of Virgo; the extended NGC 5353/4 filament, with the corresponding group at the end of it; the Canes Venatici filament just north of NGC 5353/4 filament; and the Leo II A, Leo II B, and Leo Minor filaments belonging to the Leo cloud to the northwest. To test the reliability of these filaments, we construct a series of different (SGX; SGY; SGZ) volume slices with an arbitrary depth of 4 h^{-1} Mpc along the SGY axis. Selected structures are confirmed by visual inspection of the (SGX; SGZ) projection of each slice, looking for overdense and long (i.e., filamentary) galaxy distributions. All candidate structures are present in consecutive slices. During this visual inspection of the distribution of galaxies in the (SGX; SGZ) plane, we identify five additional structures that were not reported in Kim et al. (2016) and that will enter our final filament sample. We name these respective structures the Leo Minor B, Bootes, Serpens, Draco, and Coma Berenices filaments, where the names of these filaments derive from the dominant constellation that they are in. As further discussed in Section 3.3.1, all these structures have a least one main counterpart in the V8k catalog of nearby sources and structures (Courtois et al. 2013).

Nevertheless, we stress that the goal of this work is not to provide a complete census of all filaments around Virgo. Instead, we provide a detailed characterization of the filaments that have the highest density contrast relative to the surrounding field as determined by visual inspection, including those already known in the northern hemisphere.

The 13 structures all fall within the cuboid enclosed by the following limits:

$$-13 < \mathrm{SGX}/(h^{-1}\,\mathrm{Mpc}) < 20,$$
$$2 < \mathrm{SGY}/(h^{-1}\,\mathrm{Mpc}) < 38,$$
$$-15 < \mathrm{SGZ}/(h^{-1}\,\mathrm{Mpc}) < 33.$$

These limits correspond to a more extended region in the northern hemisphere than that considered by Kim et al. (2016), which allows us to have a more comprehensive characterization of the large-scale structures around Virgo than previous studies. Note that the (SGX; SGZ) coordinate frame approximately corresponds to the plane of the sky where filamentary structures are better defined, while the SGY axis is associated with the line of sight, and thus more impacted by positional errors arising from distance uncertainties.

Similar to Kim et al. (2016), for each filamentary structure we consider an associated parallelepiped Ω in the 3D SG frame, large enough to conservatively enclose all galaxies that belong to the structure. We set the parallelepiped dimensions after the visual inspection of the filamentary structure in (SGX; SGY; SGZ) coordinates, with different projections. We then determine the filament spines by fitting the locations of the galaxies in SG coordinates. We parameterize the spine of each filament by fitting a third-order polynomial curve $\gamma{:}[0,1] \rightarrow \Omega$, such that $\vec{\gamma}(t) = \boldsymbol{a}\, t^3 + \boldsymbol{b}\, t^2 + \boldsymbol{c}\, t + \boldsymbol{d}$. Here $\boldsymbol{a}$, $\boldsymbol{b}$, $\boldsymbol{c}$, and $\boldsymbol{d} \in \mathbb{R}^3$ are the curve parameters with their origin coincident with the Sun, as this is the case for the SG (X, Y, Z) coordinate system. We then

Table 2
Detected Filaments and Spatial Extent of Their Spines

Structure	SGX (h^{-1} Mpc)	SGY (h^{-1} Mpc)	SGZ (h^{-1} Mpc)	R.A. (deg)	Decl. (deg)	L (h^{-1} Mpc)
(1)	(2)	(3)	(4)	(5)	(6)	(7)
Leo Minor F	0.59 ∼ 5.64	4.06 ∼ 6.30	−2.83 ∼ −1.77	120.27 ∼ 160.23	23.12 ∼ 52.30	7.63
Canes Venatici F	0.64 ∼ 3.97	5.89 ∼ 14.28	1.35 ∼ 4.79	197.46 ∼ 203.68	34.47 ∼ 44.13	10.53
Bootes F	5.9 ∼ 10.59	15.71 ∼ 22.83	5.91 ∼ 11.51	201.54 ∼ 216.01	43.31 ∼ 60.89	11.83
Ursa Major Cloud	0.50 ∼ 8.74	2.67 ∼ 13.95	0.12 ∼ 1.37	177.62 ∼ 186.07	34.38 ∼ 57.20	15.44
Leo II B F	2.42 ∼ 13.35	13.65 ∼ 13.97	−8.37 ∼ −4.30	131.00 ∼ 163.99	27.82 ∼ 48.15	12.67
Leo II A F	0.43 ∼ 9.18	12.25 ∼ 14.47	−14.26 ∼ −6.73	126.23 ∼ 156.97	15.79 ∼ 33.13	13.93
Virgo III F	−10.94 ∼ −5.51	11.93 ∼ 17.32	3.40 ∼ 11.09	207.31 ∼ 224.80	2.32 ∼ 5.42	11.72
Leo Minor B F	5.84 ∼ 10.83	18.28 ∼ 21.53	−7.01 ∼ −5.41	152.99 ∼ 163.15	34.13 ∼ 41.94	7.95
W–M Sheet	−9.28 ∼ −3.41	20.30 ∼ 23.27	−2.67 ∼ −1.91	183.30 ∼ 187.53	1.59 ∼ 15.15	8.45
NGC 5353/4 F	−12.57 ∼ 9.42	25.96 ∼ 27.67	0.30 ∼ 9.20	193.75 ∼ 204.04	2.09 ∼ 47.84	24.01
Serpens F	−5.48 ∼ −0.99	11.02 ∼ 17.01	9.47 ∼ 33.14	230.39 ∼ 256.6	10.82 ∼ 24.33	25.63
Draco F	13.98 ∼ 18.77	16.71 ∼ 21.50	14.90 ∼ 22.51	227.08 ∼ 259.51	58.76 ∼ 60.92	12.31
Coma Berenices F	2.15 ∼ 6.04	12.89 ∼ 38.31	−4.92 ∼ −1.89	173.06 ∼ 175.40	30.13 ∼ 35.75	26.27

Note. Column description: (1) filament name; range in SG coordinates (2–4) and in projected space (5–6) spanned by the filament spine; (7) filament spine length.

Table 3
Best-fit Parameters for the Filament Spines

Structure	$\boldsymbol{a}$ (a_x, a_y, a_z) (h^{-1} Mpc)	$\boldsymbol{b}$ (b_x, b_y, b_z) (h^{-1} Mpc)	$\boldsymbol{c}$ (c_x, c_y, c_z) (h^{-1} Mpc)	$\boldsymbol{d}$ (d_x, d_y, d_z) (h^{-1} Mpc)
Leo Minor F	−2.00 −2.00 2.00	−5.00 −5.00 −4.32	11.59 6.52 1.38	0.59 4.54 −1.90
Canes Venatici F	2.00 −2.00 2.00	−0.53 −5.00 −1.37	1.87 15.38 2.80	0.64 5.89 1.35
Bootes F	−2.00 1.08 −2.00	−5.00 −5.00 −5.00	2.62 11.03 12.28	10.28 15.71 5.91
Ursa Major Cloud	2.00 −2.00 1.52	5.00 −5.00 −1.32	1.24 18.28 1.05	0.50 2.67 0.12
Leo II B F	2.00 −2.00 2.00	3.62 1.90 5.00	5.31 0.09 −10.28	2.42 13.66 −4.30
Leo II A F	−2.00 −2.00 −2.00	−5.00 −5.00 −5.00	15.74 7.39 −0.54	0.43 12.25 −6.73
Virgo III F	2.00 2.00 −2.00	−1.61 0.10 −5.00	−5.82 3.29 14.65	−5.51 11.93 3.40
Leo Minor B F	2.00 −1.27 2.00	5.00 −5.00 −4.14	−2.24 8.77 0.55	6.07 18.28 −5.42
W–M Sheet	2.00 2.00 −2.00	5.00 5.00 1.52	−1.20 −8.67 1.00	−9.21 23.27 −2.67
NGC 5353/4 F	−2.00 2.00 −2.00	−5.00 1.32 −4.48	28.99 −4.33 15.38	−12.57 27.67 0.30
Serpens F	2.00 −2.00 2.00	5.00 −5.00 5.00	−2.89 12.74 16.66	−5.10 11.02 9.47
Draco F	−2.00 −2.00 −2.00	−5.00 −5.00 −5.00	11.25 2.50 14.56	13.98 21.21 14.90
Coma Berenices F	−2.00 2.00 1.59	−5.00 3.46 −4.17	10.04 19.95 −0.45	2.15 12.89 −1.89

Note. Each spine is parameterized with a polynomial curve γ:[0,1] $\rightarrow \Omega$, such that $\gamma(t) = \boldsymbol{a}t^3 + \boldsymbol{b}t^2 + \boldsymbol{c}t + \boldsymbol{d}$. The best-fit values of the parameters $\boldsymbol{a}$, $\boldsymbol{b}$, $\boldsymbol{c}$, and $\boldsymbol{d}$ are provided in (SGX; SGY; SGZ) coordinates for all filamentary structures considered in this work.

perform a fit by minimizing the sum of the distance squares of each galaxy in Ω to the filament spine. In Table 2 we report the spatial extent of the filaments, which span a wide range in length, between $L \sim (8-26)h^{-1}$ Mpc. In Table 3 we report the best-fit parameters of our fits to the filament spines. In Table 4 we provide different points that sample the filament spines both in projection and in the 3D SG frame. In the same table, we also report the position angles of the tangent vectors, along each filament spine.

To identify filament members we select galaxies found within $2h^{-1}$ Mpc of the spine, with the radial cut selected to minimize the contamination from the field (Lee et al. 2021; Galárraga-Espinosa et al. 2020). We verified a posteriori that all considered filamentary structures are overdense and elongated over several megaparsecs in length. Indeed, as further outlined in Section 3.3.2, the density contrast, evaluated as the ratio between the average number density of galaxies within 1 h^{-1} Mpc from the filament spine relative to the field value, ranges between $\sim 3-18$, which thus strengthens the reliability of the selected filaments.

As an example of the outcome of our procedure, Figure 4 shows the selected parallelepiped in the SG frame within which the Virgo III filament is embedded. The filament spine and filament members within 2 h^{-1} Mpc from the spine are highlighted. The latter are color-coded by their local density (see Section 4.2) to highlight density variations along the filament. These variations are also due to the presence of groups within the filament (see Section 4.1). The complexity of these structures motivates further characterization of the environment, even within filaments.

Figure 5 shows the spatial distribution of the 2118 galaxies belonging to the identified structures. Filaments are sorted by increasing distance from us, and this color scheme is adopted throughout the paper to help the reader track the different filaments. It appears evident that different filaments exhibit different properties in terms of their distance, richness, and structure. In particular, the W–M Sheet has a planar morphology, as will be further discussed in the following sections. The Leo filaments were originally classified as a single cloud by Tully (1982). Furthermore, the Ursa Major Cloud and the W–M Sheet overlap with the Virgo cluster periphery. Indeed, 418 cluster galaxies are also members of the Ursa Major Cloud (214) or the

Table 4
A Sample of Filament Points

Filament	ID_{point}	R.A. (deg)	Decl. (deg)	SGX (h^{-1} Mpc)	SGY (h^{-1} Mpc)	SGZ (h^{-1} Mpc)	PA (deg)
Virgo III	1	207.312	5.419	−5.514	11.929	3.397	92
Virgo III	2	207.875	5.398	−5.572	11.961	3.543	92
Virgo III	3	208.426	5.374	−5.631	11.994	3.688	93
Virgo III	4	208.966	5.348	−5.69	12.027	3.831	93
Virgo III	5	209.494	5.32	−5.749	12.061	3.974	93
Virgo III	6	210.012	5.289	−5.809	12.094	4.116	94
Virgo III	7	210.518	5.257	−5.868	12.127	4.257	94
Virgo III	8	211.014	5.223	−5.928	12.16	4.397	94
Virgo III	9	211.499	5.187	−5.989	12.194	4.535	94
Virgo III	10	211.973	5.15	−6.049	12.227	4.673	95
Draco	1	227.076	58.758	13.983	21.212	14.895	67
Draco	2	227.476	58.843	14.095	21.237	15.04	68

Note. Column description: (1) filament name; (2) integer index associated with the curve parameter t; (3–4) projected coordinates, (5–7) SG coordinates, and (8) position angle for the filament spine at the index reported in column (2).

(This table is available in its entirety in machine-readable form.)

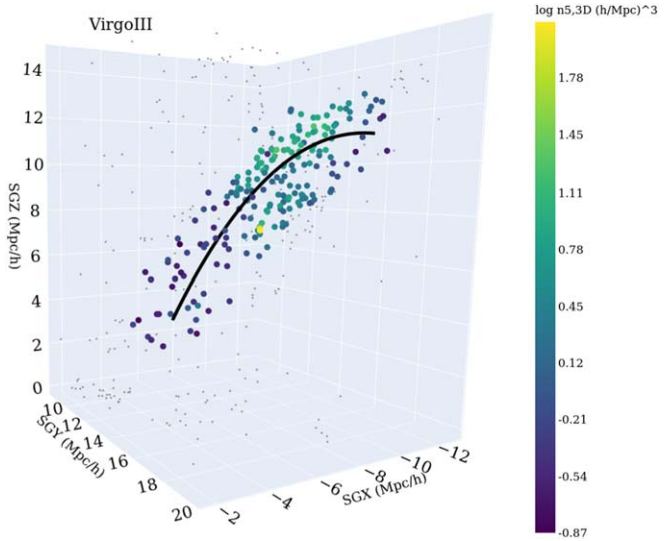

Figure 4. Galaxies in the vicinity of the Virgo III filament. Galaxies with in $2\,h^{-1}$ Mpc are color-coded by the 3D local density, and galaxies with separations greater than $2\,h^{-1}$ Mpc are shown with the gray points. The filament spine is shown with the black curve. Interactive 3D plots for all filaments are available for download from Zenodo at doi:10.5281/zenodo.6341838.

W–M Sheet (204). This is primarily due to the difficulty in unambiguously distinguishing Virgo cluster members from those of nearby correlated structures, as further discussed in previous studies (e.g., Kim et al. 2014; Kourkchi & Tully 2017).

Each filament is located at a different mean distance, and the very conservative absolute magnitude limit for the catalog was set by the most distant galaxies in the entire sample. We therefore compute an absolute magnitude limit that is appropriate for each filament (Figure 6), which might be useful for specific studies (e.g., comparing the local density of filament galaxies with the density in the surrounding field, see Figure 14). Specifically, we compute the completeness limit by computing the distance modulus from the distance encompassing 95% of galaxies in any given filament. Table 5 reports the magnitude limit and the number of galaxies above it for each filament.

3.3.1. Comparing Different Filament Determinations

As we follow the approach presented by Kim et al. (2016), we now briefly compare our results with theirs. In Table 5 we report the number of filament members identified by Kim et al. (2016) for the seven filaments in common. For these filaments the ratio of the total number of members found in this work to that reported by Kim et al. (2016) ranges between $\sim 0.6-2.3$, with a median value of 1.3. This wide range of values is due to both the different input catalogs used (our catalog has been carefully cleaned of duplicates and includes sources from additional surveys) and to the different filament membership assignments.

Memberships to filaments around the Virgo cluster can be retrieved also from the Tempel et al. (2014) catalog. However, our approach has been fine-tuned to characterize filaments specifically around Virgo, whereas Tempel et al. (2014) have searched for a large sample of filaments in the Sloan Digital Sky Survey (SDSS) over a wider field and up to larger distances (up to $450\,h^{-1}$ Mpc). Their method approximates the filamentary network using a random configuration of small segments (thin cylinders). If we cut the Tempel et al. (2014) catalog at our velocity limit ($z < 0.012$), we retain only 1281 galaxies and 774 of these are associated with 39 filamentary structures made of more than 10 galaxies. This includes filaments in the location of the Serpens, Bootes, Canes Venatici, NGC 5353/4 filaments, the Ursa Major Cloud, and the W−M Sheet, but these filaments have many fewer members. Overall their filaments are much less populated: the median number of filament members found within $1\,h^{-1}$ Mpc from the filament spine is 15. It appears therefore that to carefully characterize filaments in the local universe, it is not appropriate to apply a general approach that is optimized for a much larger ($z < 0.155$) redshift range. The above considerations motivated us to exploit a method that is tailored to the case of the local universe and specifically to filaments around Virgo.

In this context, it is worth mentioning the V8k catalog of nearby sources and structures that is discussed by Courtois et al. (2013) and is part of the Extragalactic Distance Database (Tully et al. 2009).[19] This catalog provides a census of large-scale structures in the local universe and their members. By cross-matching, via membership, the structures considered in this

[19] http://edd.ifa.hawaii.edu/index.html

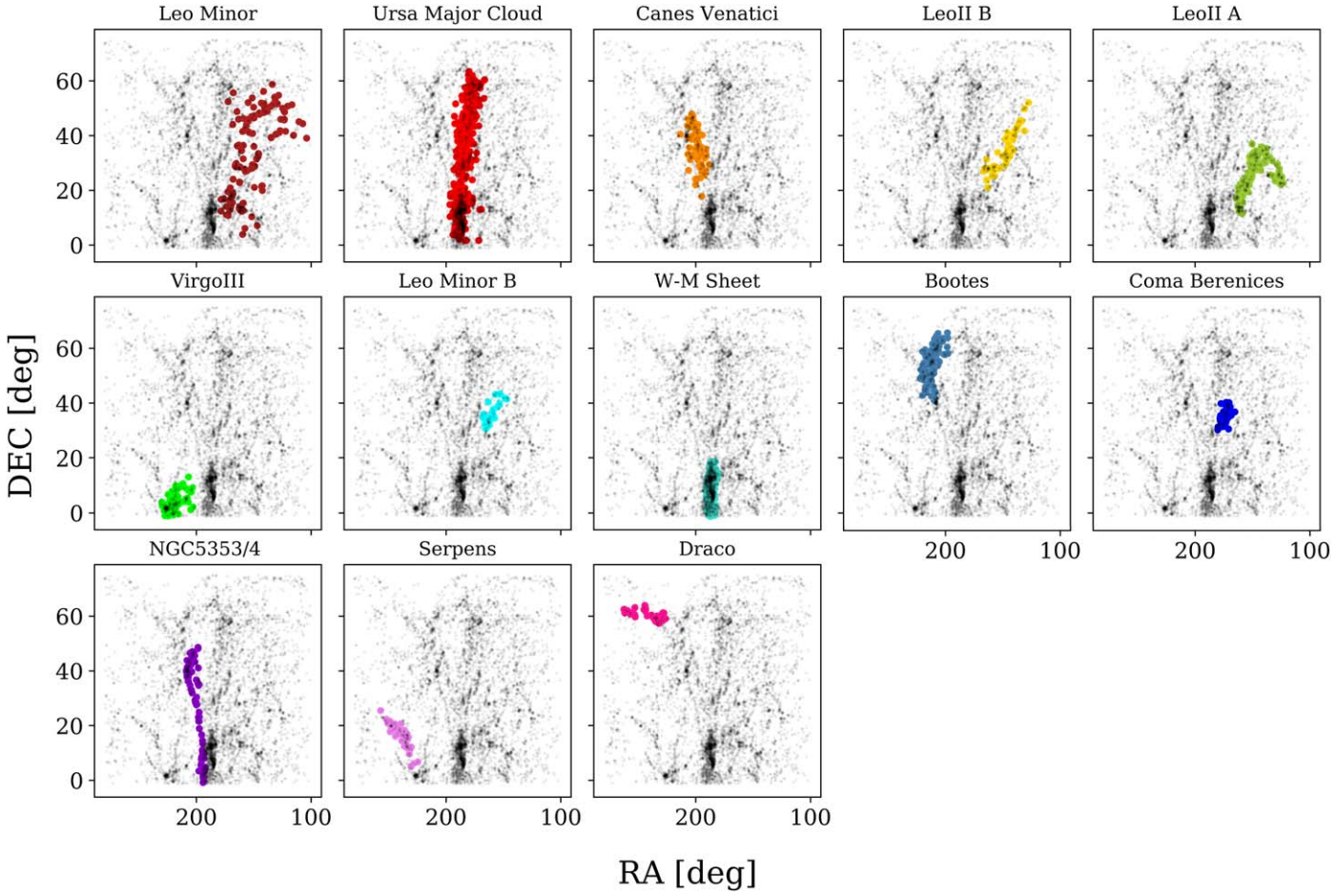

Figure 5. Spatial distribution of galaxies around the Virgo galaxy cluster. Gray points show all galaxies, colored points show galaxies belonging to the different filaments. This color scheme will be kept in all plots.

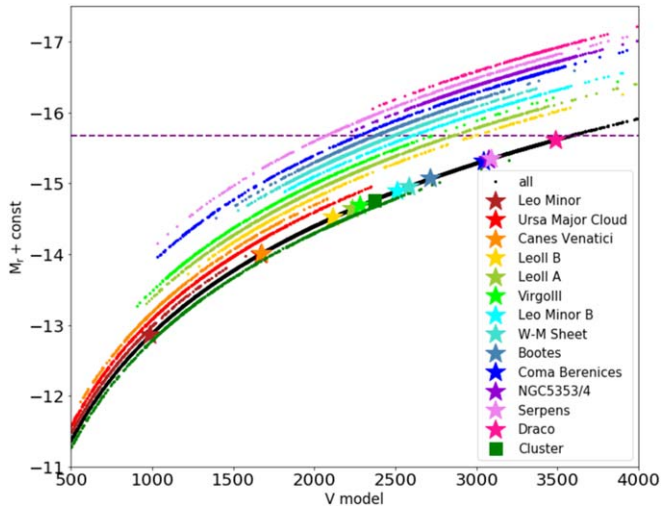

Figure 6. Absolute magnitude M_r as a function of velocity $V_{\rm model}$ (black line) and magnitude limit of the survey (horizontal dashed line). Stars represent the magnitude limit proper of each filament separately, and the green square the magnitude limit of the cluster. These limits are obtained as the magnitude including 95% of the data. For display purposes, points of the different filaments are also shown in colors, with an arbitrary vertical shift to avoid the superimposition of the points.

Table 5
Number of Galaxies in Each Filament

Structure	$N_{\rm gal}$	$N_{\rm gal}@M_{r\rm lim}$	$M_{rf,\rm lim}$	$N_{\rm gal}@M_{rf,\rm lim}$	K16
Virgo Cluster	1152	526	−15.41	570	
Leo Minor F	124	13	−12.86	62	54
Canes Venatici F	96	24	−14.01	48	51
Bootes F	169	113	−15.07	136	
Ursa Major Cloud	580	117	−14.00	217	
Leo II B F	63	28	−14.52	43	105
Leo II A F	145	53	−14.64	97	180
Virgo III F	206	115	−14.69	148	181
Leo Minor B F	39	28	−14.90	29	
W–M Sheet	345	198	−14.96	250	256
NGC 5353/4 F	133	90	−15.34	106	102
Serpens F	65	34	−15.35	39	
Draco F	48	44	−15.61	45	
Coma Berenices F	105	62	−15.32	69	
Pure field	2249	1160	...	...	
Poor groups	1086	652	...	...	
Rich groups	1626	937	...	...	
All	6780	3528	...	...	

Note. (1) Structure; (2) total number of galaxies, regardless of their magnitude ($N_{\rm gal}$); (3) number of galaxies above the survey magnitude limit ($N_{\rm gal}@M_{r\rm lim}$); (4) magnitude limit of each structure; (5) number of galaxies above the magnitude limit given in (4); (6) number of galaxies in the Kim et al. (2016) sample.

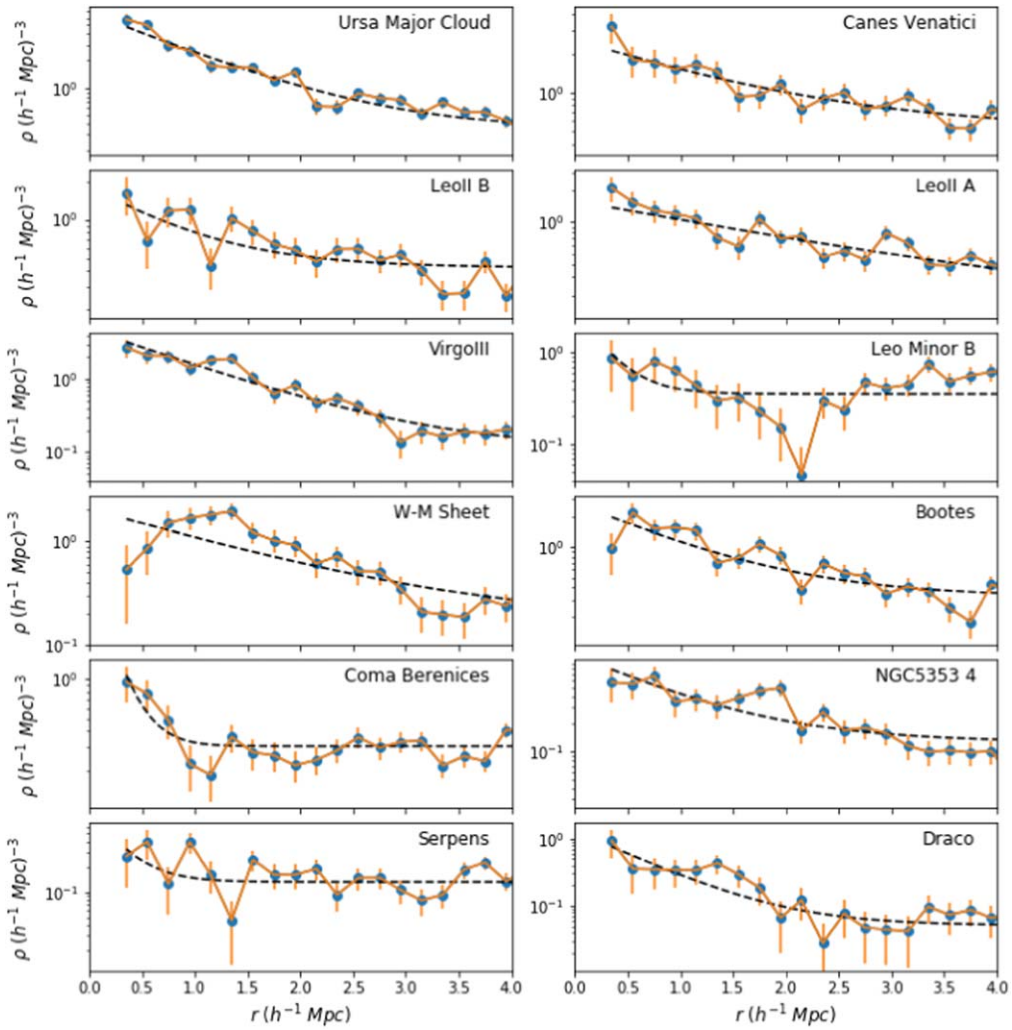

Figure 7. Galaxy density versus distance from the filament spine. Dashed lines show the exponential fit, see text for further details.

work with those listed in the V8k catalog we found that all of our structures have at least one main counterpart in V8k. This also applies to the five filamentary structures mentioned above, that are not in Kim et al. (2016) but are considered in this study. Indeed, Leo Minor B of this work is mostly matched with the Crater Cloud in V8k; Serpens with the Serpens Cloud; Draco with the Bootes cloud; Coma Berenices with the Ursa Major Southern Spur. The Bootes filament has two main counterparts in V8k: the Bootes Cloud and the Canes Venatici—Camelopardalis Cloud.

By matching the V8k galaxy catalog with ours, we also found 232 galaxies that belong to V8k structures that are not matched to any of ours, namely Cancer—Leo Cloud, Draco Cloud, V8k structure ID 322, and Ophiuchus Cloud. These structures are located along the periphery of the field around Virgo considered in our study. The presence of these clouds is not a major concern for our study. They only marginally contaminate our field sample, as in fact 128 out of the 232 (i.e., 5.6%) are classified as pure field galaxies in our work (see Section 4.1).

3.3.2. Radial Density Profiles

In this section we provide an estimate of the width and density contrast of the filaments, with the goal of better characterizing these overdense structures. Following Lee et al. (2021), we investigate how the number density of filament galaxies depends on the distance to the spine, and we calculate the density of galaxies in cylindrical shells as a function of 3D distance from the filament spine. Average densities ρ at a distance r from the filament spine are calculated within cylindrical volumes $V = \pi L[(r+\delta r)^2 - (r-\delta r)^2] = 4\pi L \delta r$ as

$$\rho(r) = \frac{N_{\rm gal}(<r+\delta r) - N_{\rm gal}(<r-\delta r)}{4\pi L \delta r}, \quad (2)$$

where L is the length of the filament (see Table 2). We increase the radius from 0.2 to 6 h^{-1} Mpc in increments of 0.2 h^{-1} Mpc, while we choose $\delta r = 0.1$ h^{-1} Mpc. We show the resulting density profiles in Figure 7. The filaments span a range of densities (the y range of individual plots varies to improve readability). When comparing densities within $\sim 1 h^{-1}$ Mpc from the spine, the Ursa Major Cloud is the densest filament and the Serpens Filament is the least dense.

Almost all profiles show a decrease in galaxy density as distance increases. The profiles describing some filaments flatten out at $r > 3h^{-1}$ Mpc (e.g., the Leo B, Coma Berenices, Leo Minor B), while others continue to decline over the full range of the radii probed (e.g., the Ursa Major Cloud, and Virgo III). These results suggest that the region around the

Table 6
Best Fits for the Density Profiles of the Filaments, Based on the Whole Sample

Structure	a (h^3 Mpc^{-3})	b (h^3 Mpc^{-3})	r_0 (h^{-1} Mpc)
Leo Minor F	2.02 ± 0.32	0.15 ± 0.26	2.67 ± 1.24
Canes Venatici F	2.05 ± 0.43	0.52 ± 0.05	1.40 ± 0.31
Bootes F	2.44 ± 0.74	0.32 ± 0.03	0.91 ± 0.21
Ursa Major Cloud	6.54 ± 0.99	0.34 ± 0.03	0.90 ± 0.09
Leo II B F	1.39 ± 0.90	0.42 ± 0.03	0.76 ± 0.38
Virgo Leo II A F	1.48 ± 0.21	0.12 ± 0.08	2.21 ± 0.59
Virgo III F	4.66 ± 0.71	0.11 ± 0.02	0.87 ± 0.08
Leo Minor B F	2.37 ± 8.89	0.35 ± 0.04	0.26 ± 0.51
W–M Sheet	1.89 ± 0.49	0.16 ± 0.06	1.42 ± 0.36
NGC 5353/4 F	1.00 ± 0.47	0.13 ± 0.02	0.83 ± 0.30
Serpens F	0.79 ± 1.84	0.13 ± 0.01	0.25 ± 0.30
Draco F	1.27 ± 0.64	0.05 ± 0.01	0.60 ± 0.17
Coma Berenices F	5.44 ± 7.56	0.31 ± 0.01	0.18 ± 0.10

Note. The density profile is parameterized as $\rho(r) = a \exp\left(-\frac{r}{r_0}\right) + b$.

filament spine is indeed where the clustering of galaxies is stronger, and they strengthen the characterization of the filament skeletons adopted in this work.

The W–M Sheet is an exception: it appears to be the only structure for which the density is not clearly declining with distance. Omitting the first two points at small radii that have large uncertainties due to small number statistics, the profile is fairly flat up to 1.5 h^{-1} Mpc and declines at larger distances. This finding is not surprising, given the planar distribution of galaxies in this structure (e.g., Kim et al. 2016).

We fit the density profiles of each filament as a function of perpendicular distance from the spine, r, with an exponential law:

$$\rho(r) = a \exp\left(-\frac{r}{r_0}\right) + b, \quad (3)$$

where a is the best-fit central density at $r \ll r_0$, above the field value; b is the best fit for the field density at large scales $r \gg r_0$; and r_0 is the exponential scale width of the filament. The best-fit parameters are reported in Table 6, while Figure 8 shows the exponential scale width r_0 and the central density contrast as a function of filament length. The central density contrast is defined as the density enclosed within $r < 1h^{-1}$ Mpc divided by the best-fit value of b. On average we find $r_0 = (0.9 \pm 0.7)h^{-1}$ Mpc. We report here the median value along with the rms dispersion around the median.[20] Interestingly, the long filaments tend to have small values of $r_0 < 1\ h^{-1}$ Mpc and low-density contrasts <5, whereas shorter filaments with $L < 17\ h^{-1}$ Mpc have a larger dispersion and reach higher values for both r_0 and the density contrast.

This analysis is based on the full catalog of ~7000 sources. This allows us to better recover the structural parameters of the filaments with a maximum signal-to-noise ratio. If we repeat the analysis using the magnitude-limited sample, we obtain similar results, but strong shot noise in several radial bins prevents us from deriving robust fits. By using the full catalog we might be biased toward observing the highest number densities for the nearest filaments. For example, the Ursa Major Cloud is nearby and very rich. Similarly, other closer filaments such as Leo Minor and Canes Venatici show high central densities. However, our key estimated parameters such as the density contrast and the scale length r_0 are fairly independent of the exact galaxy selection, as they are determined relative to the field density value, which is set at large radii $r \gg r_0$.

Our results are consistent with the theoretical expectations of Galárraga-Espinosa et al. (2020) for the local universe, who find that long filaments are thinner and less dense than shorter ones. Compared to the best fits by Lee et al. (2021) for the major Virgo III, Canes Venatici, Leo II A, Leo II B, Leo Minor, and NGC 5353/4 filaments, we find smaller central densities and higher scale length parameters. They found $r_0 < 1h^{-1}$ Mpc for all their filaments, which may be due to the fact that they adopted a different approach. In particular, they used a moving bin along the radial direction to estimate the density and fit the profile fixing $b = 0h^3$ Mpc^{-3}.

4. Additional Environmental Metrics

4.1. Groups and Field around Virgo

In Section 3.3 we focused on the determination of the filaments, neglecting the presence of other structures, e.g., galaxy groups. It is likely that groups are present both within filaments and in other field regions. As a consequence, galaxies outside of the Virgo cluster or the identified filaments are not necessarily purely field galaxies. To identify galaxy groups within our sample, we match our catalog to the environmental catalog from Kourkchi & Tully (2017). They characterized galaxy groups in our immediate neighborhood ($v_r < 3500$ km s^{-1}). Their group-finding procedure starts with the most luminous galaxy and iteratively associates galaxies that fall within its turnaround radius. The algorithm then proceeds to the next most luminous galaxy that is not already assigned to a group, and the process repeats. Their galaxy catalog involves a compilation of sources taken from the Lyon-Meudon Extragalactic Database (LEDA[21]), the 2MASS Redshift Survey, 2MRS11.75 (Huchra et al. 2012), and NED. For each galaxy in their catalog, Kourkchi & Tully (2017) provide the membership to a group and the properties of the group. Of interest for our scope is the halo mass of the hosting structure, derived from the *Ks*-band luminosity by using the M/L ratios given in their Equation (8). Therefore, Kourkchi & Tully's catalog allows us (1) identify galaxies that, regardless of their membership to any filament, belong to a group; (2) obtain a "clean" pure field sample made up of galaxies not belonging to any filaments nor associated with groups of two or more galaxies; and (3) obtain a halo mass estimate of the hosting structure for each galaxy in the sample.

We cross-match our galaxy catalog and the catalog of group galaxies of Kourkchi & Tully using a search radius of 10″, and we find 5651 matches (83% of the sample). For the 1129 galaxies with no match in the Kourkchi catalog, we assign the group membership of their closest neighbor in 3D space.

[20] Note that r_0 is overall smaller than the value of $2.3h^{-1}$ Mpc that we found in Paper I. Discrepancies might be due to both the different sample selection and the different local density estimator adopted. Indeed, Paper I considered only filament galaxies in a mass-complete sample and the fifth-nearest-neighbor density estimator. This is a good proxy for the local density, but overdense and underdense substructures within the filaments tend to increase the scatter of n_5 when plotted vs r. On the other hand, the density in Equation (2) is averaged in cylindrical shells, so that this observed scatter is limited.

[21] http://leda.univ-lyon1.fr/

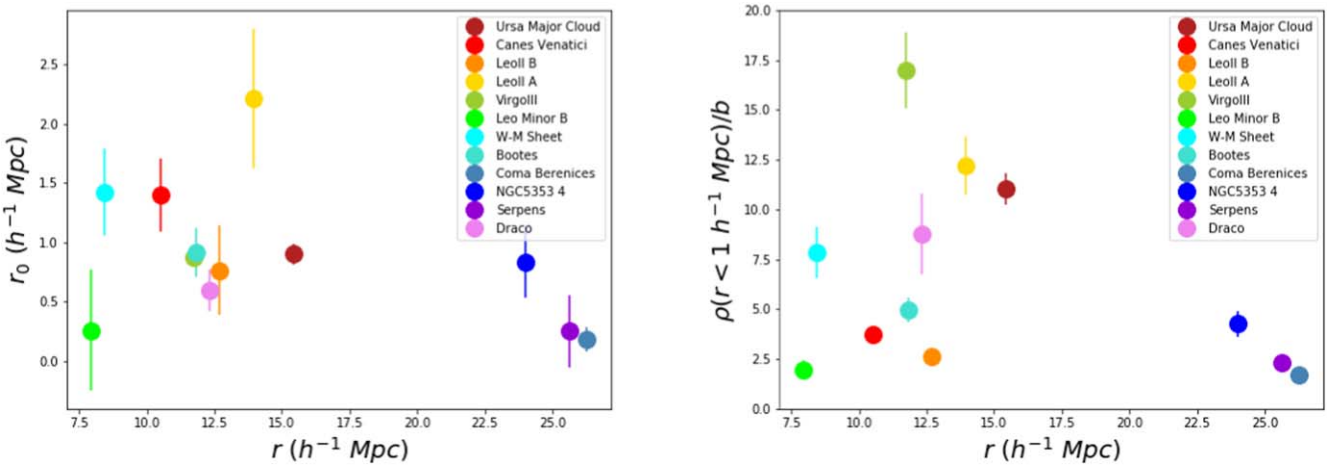

Figure 8. Scale length r_0 (left) and central density contrast (right), i.e., the ratio of the density enclosed within 1 h^{-1} Mpc to the best-fit value b at large radii, as a function of filament length.

We then classify as pure field galaxies those that are isolated based on Kourkchi & Tully's classification and do not belong to the Virgo cluster or to any filament. A total of 2249 galaxies in our catalog (1160 above the magnitude completeness limit) are pure field galaxies. Regardless of their membership in any filaments, 1086 (652 above the magnitude limit) galaxies belong to groups with $2 \leqslant N_{\rm mem} < 5$, with $N_{\rm mem}$ being the number of group members identified in the Kourkchi & Tully catalog. Hereafter, we refer to the $2 \leqslant N_{\rm mem} < 5$ groups as poor groups. We define rich groups as those with $N_{\rm mem} \geqslant 5$, and we find that 1626 galaxies (937 above the magnitude limit) belong to a rich group and are not in the Virgo cluster. The median (mean) number of members in a group is 8 (15).

Figure 9 summarizes the different environments considered, showing the overlap among the different classes. A significant fraction (33%) of galaxies in our sample are pure field galaxies, while the remaining ones are associated with megaparsec-scale overdense structures: the Virgo cluster (17%), the surrounding filaments (31%), and groups (40%). Filaments are a very heterogeneous environment: 20% of their galaxies are in common with Virgo and are thus classified as members of both the cluster and a filament (Section 3.3), 12% of them are also located in poor groups, and 36% of them are also found in rich groups. It is therefore essential to distinguish among the different global environments in which sources live if we are to understand the impact of these environments on the observed properties of the galaxy.

We then extract from Kourkchi & Tully's (2017) catalog the halo mass of the hosting system. We note that ∼20% of our cluster galaxies are not members of Virgo according to Kourkchi & Tully (2017) but instead are formally associated with lower-mass halos, with masses uniformly distributed down to $\log(M_{\rm halo}/M_{\odot}) \sim 10$. This discrepancy is due to differences in the cluster membership assignments between Kourkchi & Tully (2017) and this work, in particular in the outskirts of the Virgo, where the memberships are more uncertain. To avoid confusion and to be consistent with the Virgo membership definition used in this paper, we assign them the halo mass of Virgo $\sim 10^{15} M_{\odot}$ (Fouqué et al. 2001; Kourkchi & Tully 2017).

4.2. Local Density

In the previous sections we focused on a global parameterization of the environment. We now focus on a more local prescription in terms of local density. For each galaxy in the catalog, we compute the k-nearest-neighbor density (with $k = 5$)[22]. This is a widely used nonparametric estimate for the local environment of galaxies that is largely independent of the dark matter halo mass (see, e.g., Muldrew et al. 2012 for a review). We consider only neighbors in the catalog whose r-band absolute magnitude is $M_r \leqslant -15.7$, the completeness limit of the survey to avoid biasing our estimates toward lower values at higher distances.[23]

Specifically, local densities are computed in 3D (volume densities) in the (SGX; SGY; SGZ) Cartesian frame and in 2D (surface densities) by projecting separations onto the (SGX; SGZ) plane. The 2D density is evaluated by including galaxies within a $\Delta{\rm SGY} = 5.6 h^{-1}$ Mpc width, which corresponds to the 2σ statistical uncertainty along the line of sight at the distance of Virgo (see Figure 2). As outlined in Section 3.1 line-of-sight uncertainties are in fact of the order of ∼0.1 dex and may affect our 3D analysis.

To investigate possible biases in the density estimates, we compare the 2D versus 3D local densities in Figure 10. The two density estimates are consistent with each other once the 2D estimates are rescaled for the SGY width to convert them into 3D densities, i.e., by dividing them by 5.6 h^{-1} Mpc. The median logarithmic difference $\log(n_{5,3D}) - \log(n_{5,2D}/\Delta{\rm SGY}) = 0.06^{+0.29}_{-0.28}$ yields a negligible bias, well within the reported 1σ confidence interval. Given that results obtained with the 2D and 3D local density estimates are quantitatively in agreement, from now on we will be considering only the 3D densities.

As previously shown in Figure 3, velocity dispersion can be as high as a few thousand kilometers per second in the dense central regions of Virgo, where the gravitational potential is the highest. Model-corrected distances are thus uncertain in the

[22] Using other estimators, such as the modified 10th nearest-neighbor density (Cowan & Ivezić 2008), will not affect the results.

[23] Note that in Paper I we have not applied a magnitude cut to compute local densities. Therefore, the two measurements of local density are not directly comparable.

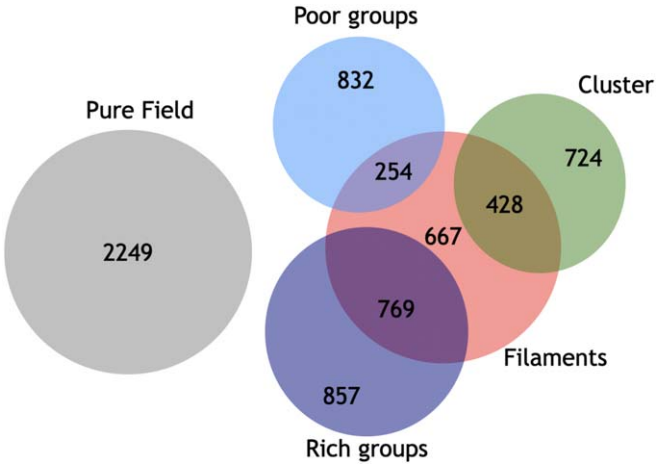

Figure 9. Euler–Venn diagram summarizing the distribution of galaxies in the different global environments.

proximity of Virgo and in particular at the caustics. This was illustrated also in Figure 2: the scatter between model-corrected and redshift-independent distances indeed increases at the distance of Virgo. This results in larger uncertainties for the local densities of Virgo members with respect to those estimated for galaxies in less dense environments. To account for a possible bias, we consider the extreme scenario where all cluster members are located at the same distance. This yields 3D local densities for Virgo cluster galaxies that are on average ∼0.4 dex higher. By collapsing the line-of-sight depth of the Virgo cluster into one distance, the associated 3D densities represent an upper limit. We discuss the implications of this further in the next sections when referring to local densities for Virgo members.

5. Comparing the Different Parameterizations of the Environment

We are now in a position to compare the different metrics adopted to define the environment: the cluster, filament, and group memberships; local densities; and the halo masses of the hosting structure. By looking for possible differences between the different environments, we can gain insights into the physical mechanisms acting at different scales.

Figure 11 focuses on the global environment: the left panel shows the halo mass distribution of the different subsamples. A correlation between halo mass and environment appears clear: the different environments span different ranges in halo masses, and the typical halo mass increases from pure field galaxies—peaking around $M_{\rm halo} = 10^{11} M_{\odot}$—to poor groups to rich groups to the cluster. The separation in halo mass between poor and rich groups is quite evident and occurs at $M_{\rm halo} \sim 10^{12.2} M_{\odot}$. This rather clear cut justifies our choice to use the richness of five members as a threshold to separate poor and rich groups.

Turning the attention to filaments, which are the focus of our analysis, we observe that they span a wide range in halo mass and the distribution is rather flat, suggesting that filaments can also host or, more generally, be linked to structures of different halo masses. About ∼400 filament galaxies are also formally associated with the Virgo cluster halo itself. This is because, as already mentioned, the Ursa Major cloud and the W–M Sheet extend up to the Virgo cluster region itself.

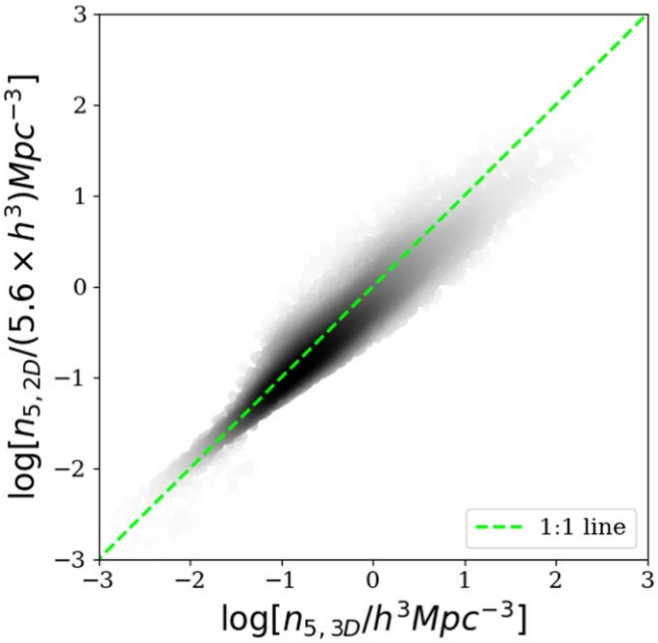

Figure 10. Comparison between the local number density estimates for the galaxies in the sample. The x-axis shows the 3D volume number densities. The y-axis displays the 2D surface densities translated into 3D volume densities, obtained dividing by the slice width $\Delta{\rm SGY} = 5.6 h^{-1}$ Mpc.

To further investigate the connection between filaments and groups, the right panel of Figure 11 shows the position of the groups identified by Kourkchi & Tully (2017) overplotted with the position of the filaments, identified by their spines for the sake of clarity. Some filaments do not contain any rich groups, while others clearly include groups, with varying incidence (from few to 50% of the galaxies). In particular, the NGC 3535/4 filament is named for the rich group where the filament seems to terminate, i.e., the filament knot (Kim et al. 2016). The Virgo III filament is an alignment of several groups (e.g., NGC 5248, 5364, 5506, 5566, 5678, 5746, and 5775) and terminates to the east with the NGC 5846 group.[24]

When investigating galaxy properties in filaments, it is therefore important to consider the presence or absence of galaxy groups. We note that the spine of the Ursa Major Cloud seems very short when compared to the distribution of member groups presented in Figure 5. This is merely a projection effect, as the closest point of the Ursa Major cloud to Earth is only 2.6 h^{-1} Mpc. At this distance, filament member galaxies, defined as those within 2 h^{-1} Mpc from the spine, are spread over 30° on the plane of the sky and appear to have a large projected distance from the southern end of the spine.

Next, we correlate the global and local environments by investigating the local density distribution in galaxies in different global environments (Figure 12). Cluster, filament, and pure field galaxies cover different density ranges, with pure field galaxies lying preferentially at lower densities and cluster galaxies at the highest ones. Filament galaxies span an intermediate range of local densities. This agrees with predictions from simulations (Cautun et al. 2014) and with what we already showed in Paper I, though for a smaller sample of filament galaxies. Nonetheless, there is a nonnegligible overlap among the different distributions, indicating that

[24] http://www.atlasoftheuniverse.com/galgrps/viriii.html

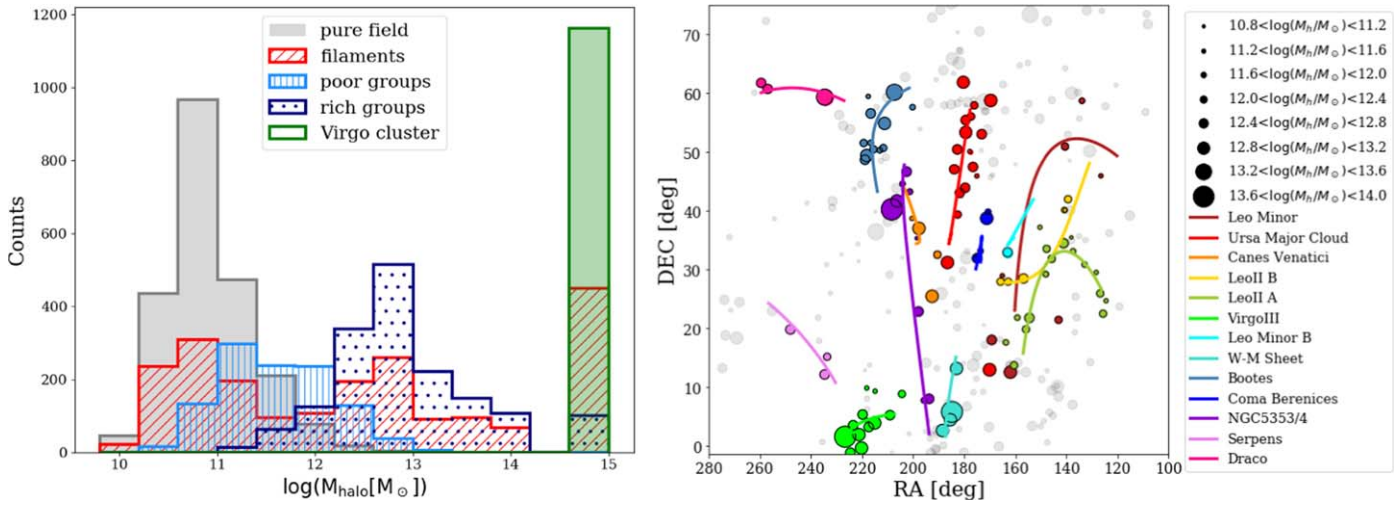

Figure 11. Left: halo mass distribution for galaxies in the different environments, using the group memberships and halo mass distributions from Kourkchi & Tully (2017). Right: spatial distribution of groups and filaments around the Virgo galaxy cluster. Shaded gray points represent all groups in the velocity range $500 < v_r < 3300$ km s^{-1} according to Kourkchi & Tully (2017). Lines represent the filament spines; colored points represent the groups that share galaxies with the corresponding filament, plotted with the same color. The size of the points scales as the halo mass.

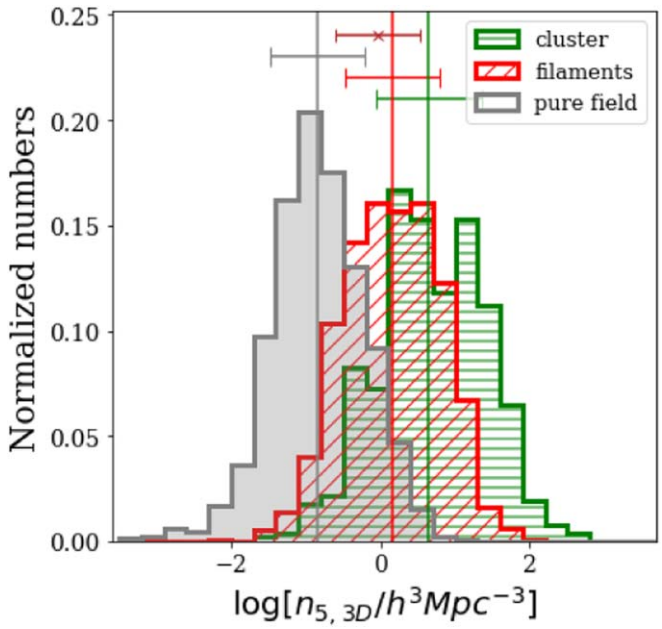

Figure 12. Volume 3D number density distribution for galaxies in the filaments (red), in the Virgo cluster (green), and in the field (gray) for galaxies above the absolute magnitude completeness limit. The reported errors are standard deviations, while the error of the means is much smaller, of the order of 0.05 dex at most. The firebrick cross and error bar show the median density for filaments when the W–M Sheet and the Ursa Major Cloud are removed from the filament sample.

there are low-density regions in the cluster and relatively dense regions in the field. The median density of the filament galaxies is considerably influenced by the Ursa Major Cloud and the W–M Sheet, which host galaxies simultaneously belonging to both the clusters and the aforementioned structures, at the high-density tail of the distribution.

The Ursa Major Cloud and the W–M Sheet are not the only structures sharing galaxies with other systems: as already mentioned, other filaments share galaxies with groups of different richness. It could therefore be possible that the large density range probed by filaments is driven by the presence/absence of groups. In Figure 13 we therefore compare the density distribution of filament galaxies (red histograms) to the density distribution of group galaxies (blue histograms) that are also in the filaments, subdivided in bins of halo mass. A shift toward larger densities when increasing the halo mass is clearly visible, confirming that filament galaxies at the highest densities are likely also members of a group.

Finally, we inspect the density distribution of the different filaments, separately, to determine if overall all filaments behave similarly or if there is a wide filament to filament variation. To increase the statistics, for each filament we use its proper completeness limit (see Table 5) and extract from the field and cluster samples only galaxies above the same limit and located up to the same distance. Figure 14 highlights that different filaments are characterized by different density distributions, taking into account both the median and the range in density.

To conclude, the main result of this section is that even though the local and global parameterizations of the environment agree qualitatively with each other, there is no clear one-to-one correlation between the two. This demonstrates that contrasting the variation of galaxy properties as a function of the global and local environment separately is important in identifying the acting physical mechanisms.

6. Properties of the Galaxies in Different Environments

In this section we provide an overview of the properties of galaxies located in different environments. We consider the de Vaucouleurs morphological parameter (simply called morphology from now on, Section 6.1) and the presence of bars (Section 6.2). These parameters are taken from the HyperLeda catalog. Above the completeness magnitude limit $M_r = -15.7$, 3485/3530 galaxies have a value of morphology, and 3450/3530 have information on the presence or absence of a bar.

The HyperLeda catalog also provides information on the position angle of each galaxy. Similarly to Paper I, we measure the projected orientation $\theta_{\rm alignment}$ between the major axis of each filament galaxy and the direction of the filament spine, estimated at the point of minimum distance from the galaxy. The alignment is thus the galaxy position angle, $0^\circ \leqslant \theta_{\rm alignment} \leqslant 90^\circ$, with

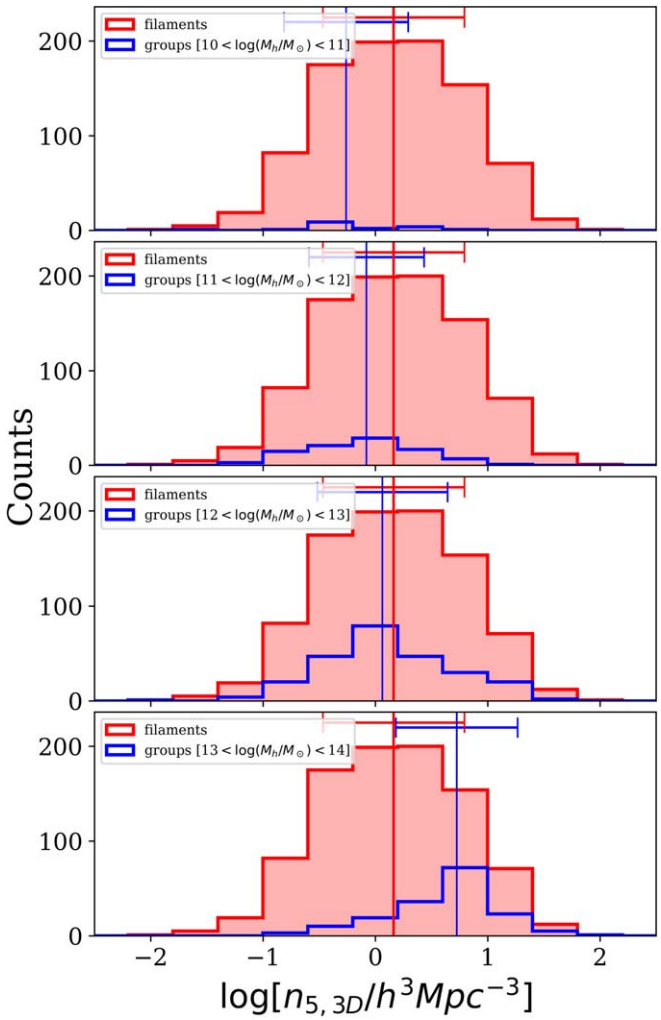

Figure 13. Volume number density distribution for galaxies in groups of different halo masses and in filaments (blue histograms). Red histograms show the overall distribution for filament galaxies. The solid vertical lines show the median values of the distributions, while the error bars show the 1σ uncertainties.

respect to the projected orientation of the filament in the plane of the sky. In Section 6.3 we search for possible features in the alignments of galaxies in the filaments.

6.1. Morphologies

We investigate the morphological properties of galaxies as a function of their global environments (cluster, filaments, groups, field) and the associated local parameterization in terms of local densities. We will distinguish galaxies between early type (de Vaucouleurs morphological type $T < 0$, ET) and late type ($T \geqslant 0$, LT).

6.1.1. Morphology and the Environment

Figure 15 shows the incidence of each morphological type in the different global environments. As seen in the left panel, there is a clear dichotomy in the morphology of cluster and pure field galaxies, which have preferentially early- and late-type morphology, respectively.

Galaxies in poor groups follow quite closely the trend of the pure field galaxies, while overall rich groups and filaments have intermediate behaviors, with an excess of ET galaxies with respect to the pure field, and an excess of LT galaxies with respect to the cluster.

To understand if the trends in filaments depend on the presence/absence of massive groups within them or if filaments are truly a site of transformations, in the right panel of Figure 15 we compare the morphological distribution of galaxies only belonging to filaments to those belonging simultaneously to a filament and a rich group. Filament galaxies that are not in rich groups exhibit a bimodal morphological distribution: galaxies have either a very ET or LT morphology, while intermediate values are less favored. The observed excess of ET galaxies with respect to the pure field suggests that filaments induce a morphological transformation, even when groups within them are not included.

In contrast, galaxies of rich groups, either in filaments or not, show a fairly uniform distribution in morphological type, suggesting that rich groups act as the main driver for the suppression of the LT galaxy excess that is typical of the pure field. The fraction of the earliest type is the highest when galaxies are both in rich groups and filaments, suggesting that the combination of the two environments promotes transformations. When considering poor groups, we verified that differences between galaxies in both filaments and groups and only in filaments disappear, indicating that poor groups do not play a major role in inducing morphological transformations.

The results above highlight that the dependence of morphology on the global environment is complex. This is particularly true for filaments, which span four orders of magnitude in local density. We therefore look for any morphological trends as a function of local density. Figure 16 shows the median morphological T-type plotted against the median local density for each filament, separately. Cluster and pure field values are shown for comparison. Overall, even though the scatter is large, the two quantities are anticorrelated: denser structures tend to be dominated by ET galaxies. Filaments are intermediate between the pure field and the cluster, and a large filament-to-filament variation is detected on both axes. A few structures, i.e., Leo Minor, Canes Venatici, Leo Minor B, and Serpens, show almost no ET galaxies. These are filaments with only a few groups (Figure 11, right) and with the lowest average densities. In contrast, Virgo III, Ursa Major Cloud, and the W–M Sheet have on average the highest local densities, higher fractions of ET galaxies, and are rich in groups. We remind the reader that Virgo III is an alignment of several groups, while both the W–M Sheet and the Ursa Major Cloud are connected to the Virgo cluster itself. This may explain at least partially their higher local densities and the prevalence of ET galaxies.

To conclude, the above results show that the ET galaxies are largely present already in filaments, which support the scenario that morphological transformations may occur well before galaxies fall into the cluster core.

6.1.2. Morphological Fractions in the Different Environments

We now quantify the variation of the morphological fraction with the environment, more specifically in terms of the LT fraction, i.e., the number of galaxies with an LT morphology over the total. The left panel of Figure 17 shows that, considering the different global environments, the fraction monotonically increases from the cluster (∼40%) to the pure field (>80%), while filaments have an intermediate fraction (60%). Interestingly, galaxies that are both in groups and filaments have a lower probability of being LT than both galaxies in groups only and

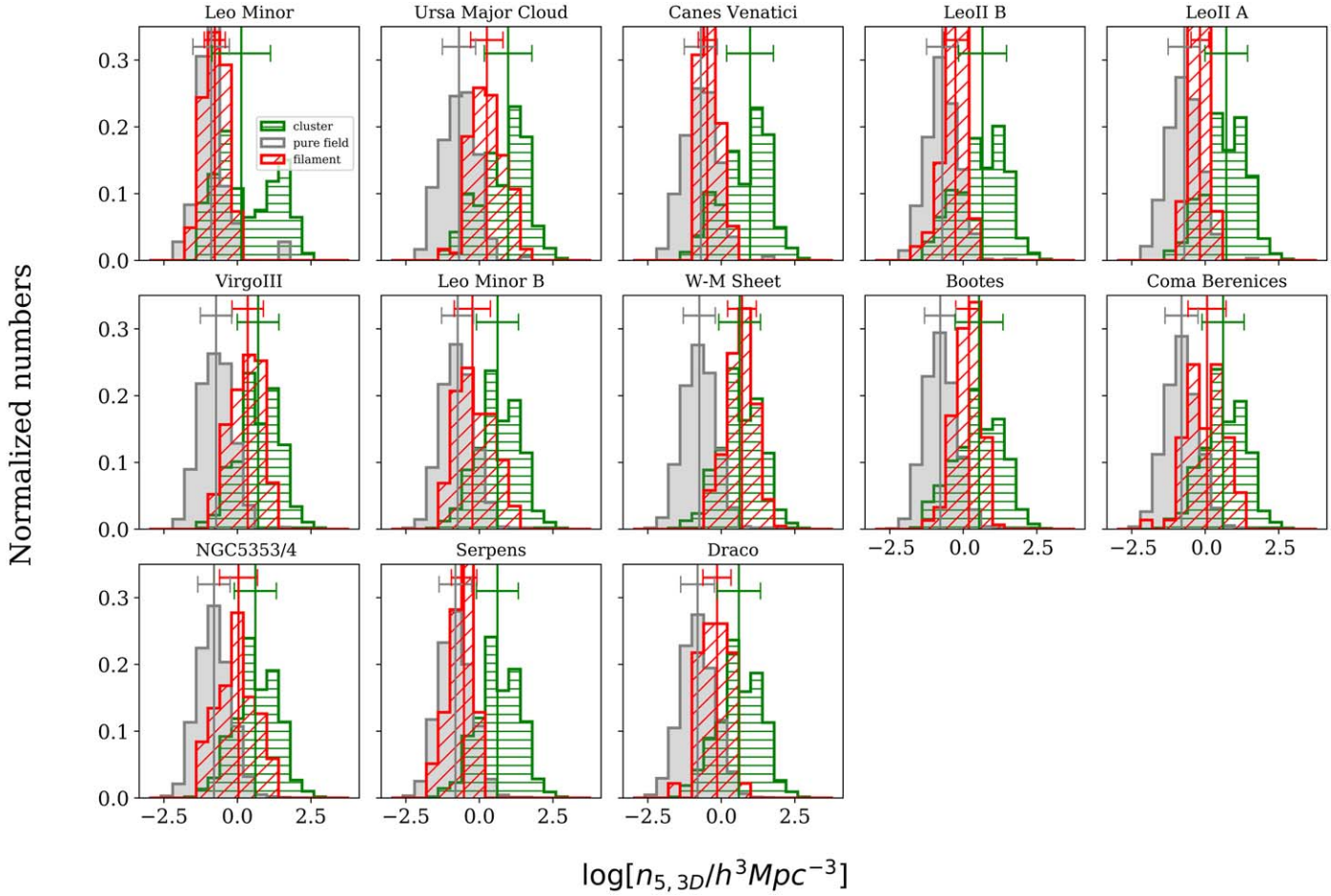

Figure 14. Volume number density ($n_{5,3D}$) distribution for galaxies in each filament separately (red). For each filament, the proper absolute magnitude limit (see Table 5) has been adopted to increase the statistics. For comparison, the distributions of galaxies in the Virgo cluster (green) and in the field (gray) are also reported, above the same completeness limit and limiting the sample to the same velocity. Vertical lines represent median values, horizontal lines the standard deviation, representing the scatter of the distribution.

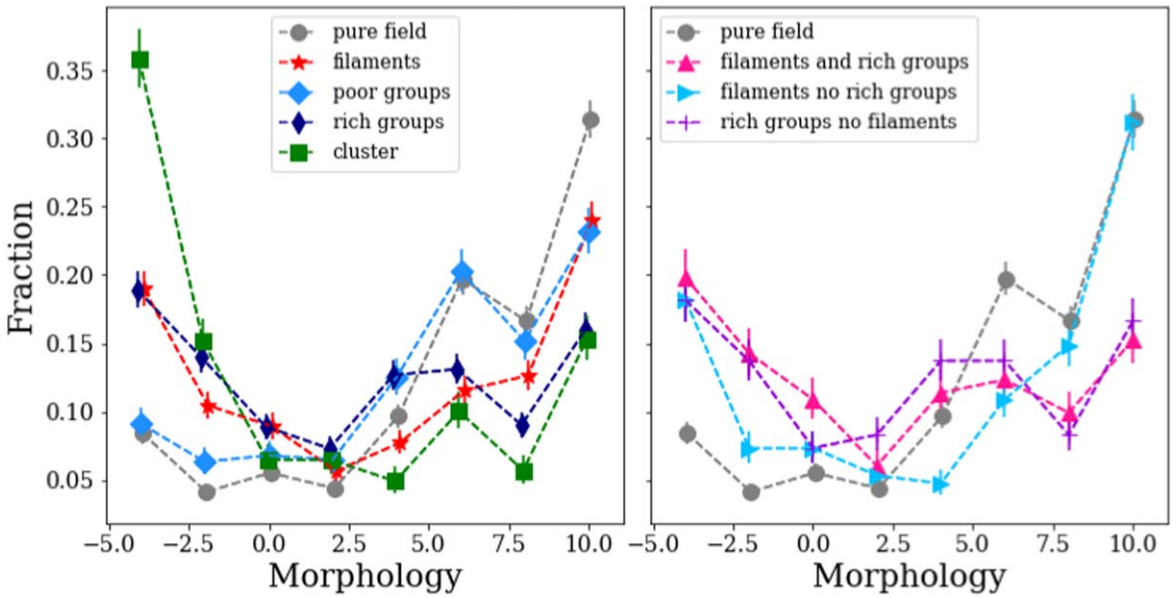

Figure 15. Fraction of galaxies of different morphological types in the different environments, as described in the legend. A small arbitrary horizontal shift has been applied to the points for the sake of clarity.

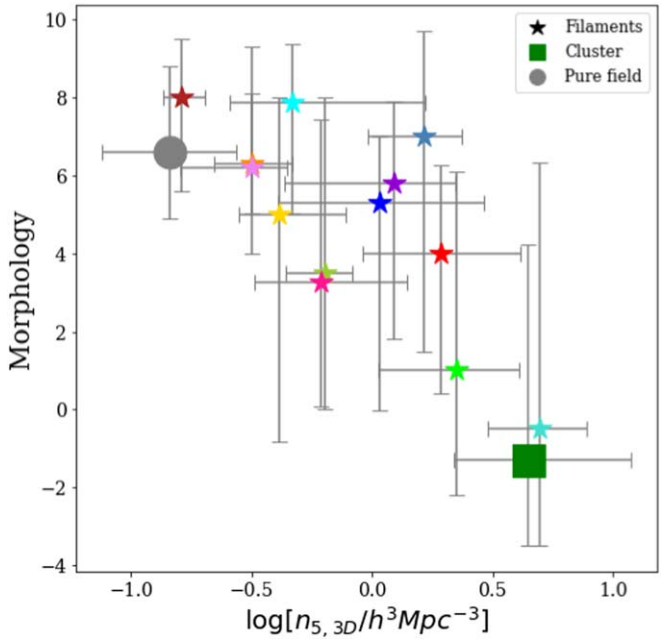

Figure 16. Median morphological parameter for filaments (colored stars), pure field (gray point), and the Virgo cluster (green square). Error bars represent 1σ dispersion. The color code for filaments is the same as in Figure 5.

sources in filaments only. This result again points to the scenario according to which both filaments and groups affect morphology, separately, and their effect is amplified for galaxies simultaneously in both environments. We verified that we obtain similar results when considering the halo mass of the hosting structure, with the fraction of LT decreasing with increasing halo mass.

We are now in the position to investigate the so-called morphology–density relation (Dressler 1980). This relation was first established for clusters only, then groups (Postman & Geller 1984), and we now inspect it also in other global environments (central and right panels in Figure 17) to determine which environmental definition plays the major role. In each global environment taken separately, we see a decline of the LT fraction with increasing density. Nonetheless, the global environment does play a role in shaping the LT fraction: at a fixed density, the LT fraction increases from cluster, rich groups, filaments, poor groups, and to the pure field. As discussed in Section 4.2, local densities in Virgo are more uncertain than for the other global environments. We have therefore computed the cluster morphology–density relation using the density estimates obtained assuming that all cluster galaxies are at the exact same distance. This provides a conservative upper limit on the local density estimates, as the distance along the line of sight between cluster galaxies is artificially set to zero. This compression of distances yields local densities that are $\sim$0.4 dex higher, on average, than the actual estimate for the local density of cluster galaxies. The right border of the green area in Figure 17 shows the relationship derived when using the upper limits on local density. Even assuming the upper limits as true values for the local density of cluster galaxies, their associated LT fractions only tentatively reach those of filament galaxies. This result shows that uncertainties associated with the local densities of cluster galaxies do not impact our results: the observed differences between the global environments considered remain.

In the right panel of Figure 17 we look for other possible differences when considering filament and rich group galaxies in all possible combinations. While these environments showed different morphology distributions (Figure 15 right), these differences disappear in the LT fraction versus density plot. This suggests that the overall density–morphology relation is similar for groups and filaments, even if there are measurable differences in the morphological composition of their galaxy populations.

Finally, we investigate the dependence of LT fraction on the distance to the cluster and to the filament spines (plots not shown). The LT fraction of filament, field, and group galaxies is flat, up to the largest clustercentric distances ($\sim 30\,h^{-1}$ Mpc). A similarly flat behavior is observed as a function of the distance to the filament spines for filament members. In particular, to appreciate a trend (if any) we should reach larger distances from the filament spine than 2 h^{-1} Mpc, i.e., the radius up to which filament membership is assigned. This is a consequence of the fact that at larger distances we have the strongest density contrast with respect to the central regions close to the filament spines.

6.2. Bars

We now investigate the presence of bars in our sample. In this subsection only, we conservatively exclude both elliptical and irregular galaxies because they typically do not show evidence of bars. We thus limit ourselves to lenticular and spiral galaxies (i.e., $-3 \leqslant T \leqslant 8$), and we consider as barred galaxies those sources that are classified as barred by HyperLeda.

In Figure 18 we investigate the bar fraction as a function of the global environment (left panel) and as a function of the local density (center) and morphology (right), considering each filament separately. There is a light but rather systematic decrease in the bar fraction from the cluster, to filaments, to the pure field. This trend might be at least partially due to local density. As illustrated in the central panel, a mild trend toward a higher bar fraction for increasing local density is observed. Filaments are intermediate between the cluster and the pure field, showing bar fractions of $\sim$0.35 and $\sim$0.6 for the field and cluster, respectively. In contrast, as shown in the right panel of Figure 18, we do not observe any clear trend of the bar fraction as a function of the average/median morphology.

In Paper I we showed that the fraction of galaxies with star formation below the main sequence monotonically increases in filaments with increasing local density. The observed trend for the bar fraction as a function of local density could thus be related to the fact that the presence of bars may favor the cessation (quenching) of star formation, as suggested by a number of studies (e.g., James & Percival 2016; Newnham et al. 2020; Fraser-McKelvie et al. 2020).

A large scatter is nonetheless observed when comparing the different filaments, with the nearby ones preferentially showing the highest bar fractions. An example is the nearby Leo Minor filament, which has a very high bar fraction of $\sim$0.8 and low average density, while its galaxy population is mostly composed of LT galaxies. Note, however, that these results are based on only 7 galaxies, while the number of barred galaxies in the other filaments range from 15 to 82. In addition, we note that the bar identification is a very delicate task and that the bar detection in HyperLeda has been attempted only for a small fraction of galaxies, mostly those larger than $1'$ of diameter, which may cause a possible bias in the determination of the bar fraction.

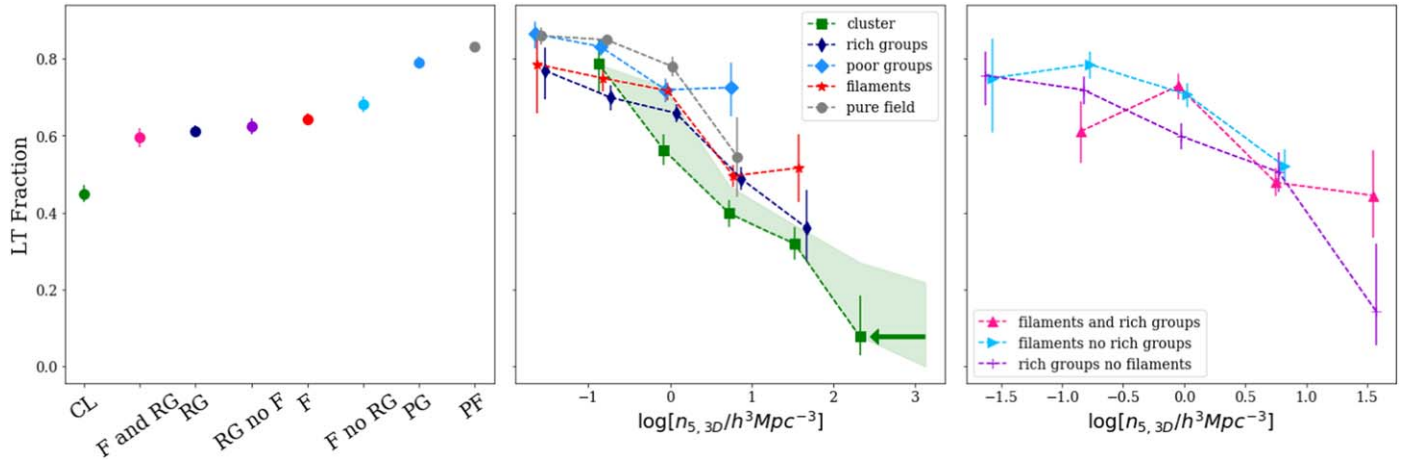

Figure 17. LT fraction as a function of different environments (left) and local density (center, right). Different environments are considered in the left panel: cluster galaxies (CL), filament galaxies (F), pure field galaxies (PF), galaxies in rich (RG) and poor (PG) groups, as well as a combination of these classes, at intermediate environments. In the central panel, the right border of the green dashed area defines the conservative upper limit to the local density for Virgo cluster galaxies. A small arbitrary horizontal shift has been applied to the points for the sake of clarity.

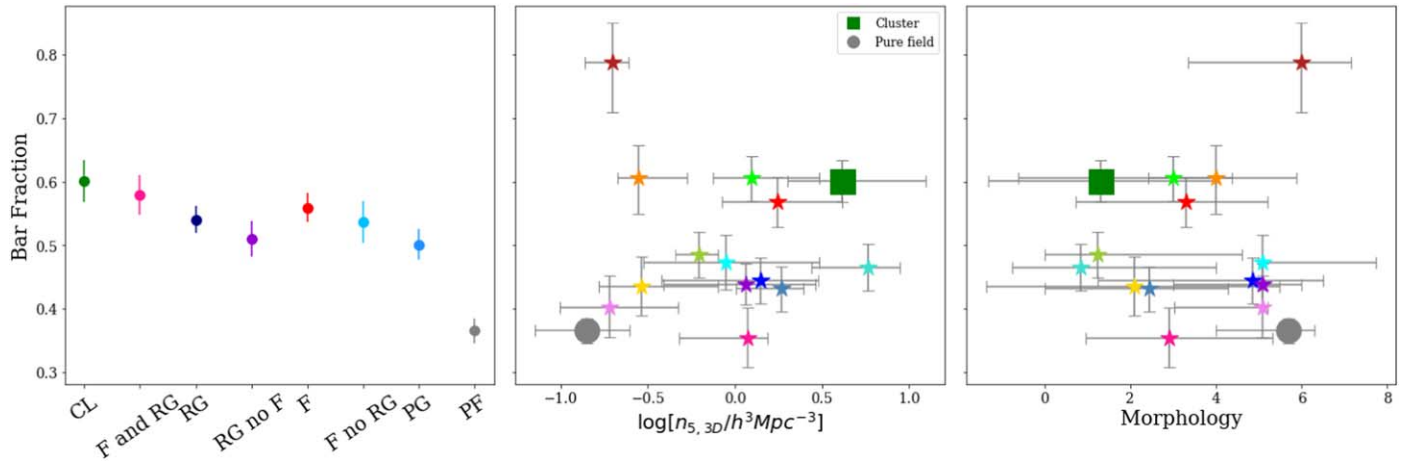

Figure 18. Bar fraction as a function of the environment (left), local density (center), and morphology (right). Only lenticular galaxies and normal spirals are considered; see text for details. For the left panel, the different environments are reported as in Figure 17 (left). In the central and right panels, filaments (colored stars), pure field (gray point), and the Virgo cluster (green square) are distinguished. The color code for the filaments is the same as in Figure 5.

Furthermore, the classification likely comes from optical images, while bars are better seen in the infrared (Eskridge et al. 1999).

Overall, from our analysis, we find that bars are found in 56% of lenticular and spiral galaxies in filaments. The fractions are distributed as follows: 41% (39/95) for lenticulars ($-3 \leqslant T < -1$), 59% (73/124) for ET spirals ($-1 \leqslant T < 3$), and 60% (154/257) for LT spirals ($3 \leqslant T \leqslant 8$). The total fraction of galaxies with strong or weak bars should be closer to 2/3 as SA, SAB, and SB galaxies are in proportions of 1/3 each (e.g., Eskridge et al. 1999). It is thus likely that some of the galaxies in our sample are misclassified as nonbarred as a consequence of the observational uncertainties mentioned above.

Nevertheless, our bar fractions are fairly in agreement with those found for galaxies in the local universe, in the range ∼(45–60)% (Marinova & Jogee 2007; Reese et al. 2007; Barazza et al. 2007). In particular, Aguerri et al. (2009) considered the redshift range $0.01 < z < 0.04$ and found fractions equal to 29%, 55%, and 54% for lenticulars, and ET and LT spirals, respectively. To derive these fractions the authors analyzed the *r*-band images of a large sample of galaxies in SDSS down to an absolute magnitude limit of $M_r = -20$, a magnitude limit that is brighter than what we use in this work. By using the same magnitude cut adopted by the authors we obtain even higher fractions for all considered classes, with an overall bar fraction of 71%. These differences highlight the difficulty in assessing an absolute bar fraction that is independent of the sample selection, the images used, and the method adopted to detect the bars.

6.3. Galaxy Alignments with Respect to the Filament Spines

We conclude the overview of galaxy properties by investigating the alignment of filament galaxies with respect to the filament spine.

Overall, for each of the filaments, we verified that the distribution of $\theta_{\rm alignment}$ is fairly uniform, with mean alignments around 45°. Previous studies (Tempel et al. 2013; Tempel & Libeskind 2013b; Hirv et al. 2017; Codis et al. 2018; Chen et al. 2019; Welker et al. 2020; Kraljic et al. 2021) found that the spin axis of ET and LT galaxies is preferentially perpendicular and parallel, respectively, to the filaments. The expected difference can be ultimately related to the different

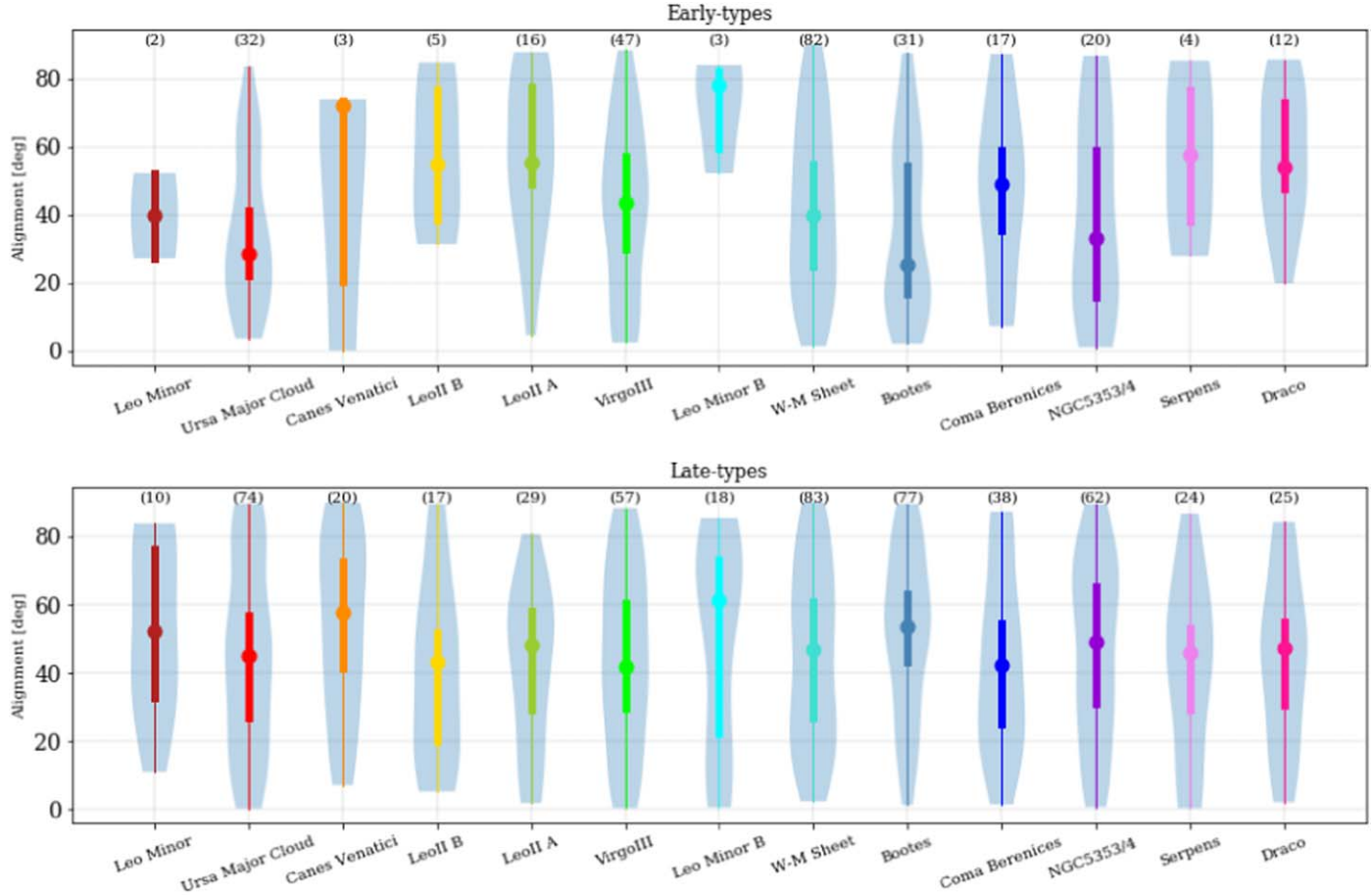

Figure 19. Violin plots of the alignments $\theta_{\rm alignment}$ for ET (top) and LT (bottom) galaxies in filaments. For each filament, medians and the interquartile ranges are also shown with circles and thick bars, respectively. We report in parentheses the number of galaxies in each filament.

assembly histories of ET and LT galaxies. ET galaxies are thought to be predominantly formed via major mergers. During these events, the rotation axis of the resulting galaxy tends to be perpendicular to the merger direction. For LT galaxies, the assembly primarily occurs via the winding of flows, and the alignment of angular momentum with the filament spine is related to the regions outside filaments, namely sheets, where most of the gas is falling in from (Tempel & Libeskind 2013b).

In Figure 19 we therefore inspect the alignment distributions for LT and ET galaxies, separately. Data distributions are shown in terms of violin plots, which give the probability density of the data at different values, smoothed by a kernel density estimator. Unlike bar graphs with means and error bars, violin plots show the distribution of all data points. The shape of the violin displays the frequencies of values: the thicker part of the violin shape means that the values in that y-axis section of the violin have a higher frequency, and the thinner part implies lower frequency. Violin plots also highlight the maximum extension of the data, and the presence of different peaks, their position and relative amplitude. The maximum width of each violin is set the same for all galaxies, for display purposes.

While for LT galaxies the average alignments scatter around 45° for all filaments, for ET galaxies we do see a higher filament by filament variation, with median $\theta_{\rm alignment}$ values ranging from ∼20° to 80°. This large scatter may be due to the limited number of ET galaxies in each filament, which is reported in parentheses above each violin in the Figure.

We did not find any statistically significant difference when comparing the overall distribution of $\theta_{\rm alignment}$ of ET and LT galaxies with the Kolmogorov–Smirnov test. This is partially at odds with the aforementioned studies; however, the absence of a significant difference may be due to uncertainties associated with the determination of the alignment angle, as the analysis is done in projection and relies on the position angles of the galaxy and the filament, estimated locally, which are both uncertain. Similarly, no difference has been found in $\theta_{\rm alignment}$, when considering barred and nonbarred galaxies, separately. No trend of $\theta_{\rm alignment}$ as a function of distance to the filament spine has been found.

7. Summary and Conclusions

We have presented a comprehensive catalog of galaxies extending up to ∼12 virial radii in projection from the Virgo cluster, with the intent of characterizing the complex network of filamentary structures around Virgo and investigating the role of filaments in galaxy evolution. We select spectroscopically confirmed galaxies from HyperLeda, the NASA Sloan Atlas, NED, and ALFALFA, assembling a sample of galaxies in the region $100° < \rm R.A. < 280°$, $-1.3° < \rm decl. < 75°$, with recession velocities in the range $500 < v_r < 3300$ km s^{-1}. These cuts ensure that both Virgo and its main filaments in the northern hemisphere are included. The final catalog contains 6780 galaxies, 3528 of which are brighter than the absolute magnitude limit $M_r = -15.7$ ($\simeq M_r^\star + 3$, Blanton et al. 2005).

To characterize the environment around Virgo, we adopt a number of parameterizations that trace different scales. By exploiting a tomographic approach, we recover 13 filaments, spanning several megaparsecs in length.

We then assign filament memberships, relying on the 3D distance of the galaxies from the filament spines, which we release for all 13 considered filamentary structures. We also identify the cluster members both in the 3D SG coordinate frame and also consider the cluster region in phase space.

To further characterize the environments of our catalog galaxies, we match our sample to Kourkchi & Tully's (2017) group catalog to select galaxies in groups and extract for each galaxy of the sample the halo mass estimate of the hosting structure. Finally, we quantify the local environment using surface (2D) and volume (3D) local densities in terms of the fifth-nearest neighbors. We make available the catalogs of galaxies and of the aforementioned environments.

We then characterize galaxy morphology and spin alignment of galaxies in filaments and discuss the different parameterizations of the environment. The main results of our analysis are:

1. By fitting an exponential model to the distribution of galaxies, averaged in cylindrical shells around each filament spine, we find that long $>17\,h^{-1}$ Mpc filaments have low characteristic radii $r_0 < 1\ h^{-1}$ Mpc (along the direction perpendicularly to the filament spine) and the lowest density contrasts with respect to the field. Shorter filaments have a larger range of values of both the density contrast and characteristic radius and extend to higher values in each.
2. Filament galaxies span a wide range of ~ 4 dex in both local density and halo mass of the hosting structure (e.g., group). Values range at the low end from those typical of the field to values found in the Virgo cluster at the high end. The high dispersion found for the filaments is ultimately due to the large filament to filament variation and to the fact that some filaments are very rich in groups, while others are poorer.
3. A decline of the LT fraction with increasing local density is observed in all considered global environments (field, filaments, groups, and cluster). At fixed local density, filaments appear to be an intermediate environment between the field and the cluster, with a decline resembling that of rich groups. The local density alone is thus not sufficient to explain the dependence of the LT fraction with the megaparsec-scale environment.
4. The average fraction of barred galaxies decreases from the highest-density regions of the cluster to the field at the lowest density. Filaments show an intermediate and broad range in the fraction of barred galaxies, with a large filament to filament variation, which reflects the large dispersion for filament galaxies observed also in local density and morphology.
5. We find no clear dependence of the projected orientation of the galaxy major axis with the filament spine for either ET or LT galaxies. Similarly, we did not find any clear trend for the considered properties of filament galaxies as a function of their distance to the spines. However, it is important to note that we only consider filament members to be those galaxies closer than 2 h^{-1} Mpc from the filament spine. While this radius allows us to minimize contamination from field galaxies, it does make it hard to assess whether trends would exist if we included galaxies at larger distances.

The authors thank the hospitality of the International Space Science Institute (ISSI) in Bern (Switzerland) and of the Lorentz Center in Leiden (Netherlands). Regular group meetings in these institutes allowed the authors to make substantial progress on the project and finalize the present work.

G.C. acknowledges financial support from the Swiss National Science Foundation (SNSF). B.V. acknowledges financial contribution from the grant PRIN MIUR 2017 n.20173ML3WW_001 (PI Cimatti) and from the INAF mainstream funding program (PI Vulcani). R.A.F. gratefully acknowledges support from NSF grants AST-0847430 and AST-1716657. G.H.R. acknowledges support from NSF-AST 1716690.

This research has made use of the NASA/IPAC Extragalactic Database (NED) which is operated by the Jet Propulsion Laboratory, California Institute of Technology, under contract with the National Aeronautics and Space Administration. We acknowledge the usage of the HyperLeda database.[25] This research made use of Astropy,[26] a community developed core Python package for Astronomy (Astropy Collaboration et al. 2013, 2018), matplotlib (Hunter 2007), and TOPCAT (Taylor 2005).

Appendix
Catalogs

With this paper, we release a number of catalogs: the main galaxy catalog, the catalog of the environmental properties, and the catalog with the filament spines. The main galaxy catalog is shown in Table 7 for a subsample of 10 galaxies. The table is presented in its entirety in the online version of the article. The columns indicate:

1. Column (1)—VFID, a unique serial number, with galaxies sorted by decl. from north to south;
2. Columns (2) and (3)—R.A. and decl. at epoch J2000 (in degrees);
3. Column (4)—v_r heliocentric velocity (units of km s^{-1});
4. Column (5)—$V_{\rm cosmic}$ cosmic recession velocity (units of km s^{-1}) obtained from a redshift-independent distance from Steer et al. (2017) when available or from $V_{\rm model}$ as described in Section 3.1;
5. Column (6)—$V_{\rm model}$ model recession velocity (units of km s^{-1}) obtained from the Mould et al. (2000) model, as described in Section 3.1;
6. Column (7)—HyperLeda name;
7. Column (8)—NED name;
8. Column (9)—PGC ID;
9. Column (10)—NSAID from the v0 catalog;
10. Column (11)—NSAID from the v1 catalog;
11. Column (12)—*Arecibo Galaxy Catalog* (AGC) name;
12. Column (13)—Boolean flag, where True indicates that the galaxy has a CO observation from Paper I;
13. Column (14)—Boolean flag, where True indicates that the galaxy is in the ALFALFA α.100 catalog (Haynes et al. 2018).

Galaxy environmental properties are listed in Table 8 for a subsample of 10 galaxies, while the table for the total sample is given in the online version of the article. The columns indicate:

[25] http://leda.univ-lyon1.fr
[26] http://www.astropy.org

Table 7
Main Catalog with Cross IDs

VFID	R.A. (deg, J2000)	Decl. (deg, J2000)	v_r (km s^{-1})	$v_{\rm cosmic}$ (km s^{-1})	$v_{\rm model}$ (km s^{-1})	HL Name	NED Name	PGC	NSA V0	NSA V1	AGC	CO	A100
(1)	(2)	(3)	(4)	(5)	(6)	(7)	(8)	(9)	(10)	(11)	(12)	(13)	(14)
3000	165.930807	28.88713	708	1189	644	NGC 3510	NGC 3510	33408	100677	472983	6126	False	True
3001	149.190405	28.82596	510	687	495	UGC 05340	UGC 05340	28714	136251	623560	5340	False	True
3002	194.776643	28.81178	998	1177	1177	PGC 1846725	WISEA J125906.48 + 284842.6	1846725	89104	427578	−999	False	False
3003	157.778262	28.79659	1425	1732	1732	NGC 3265	NGC 3265	31029	107764	497691	5705	True	True
3004	129.582068	28.78993	2669	2842	2842	PGC 3095094	WISEA J083819.66 + 284723.7	3095094	135383	622813	−999	False	False
3005	181.303258	28.78191	3153	3395	3395	UGC 07072	UGC 07072	38268	102495	478264	7072	False	True
3006	250.089288	28.76552	976	1291	1291	SDSS J164021.43 + 284555.9	SDSS J164021.43 + 284555.9	4123676	69715	343115	262737	False	True
3007	225.279839	28.76086	1821	2158	2158	SDSS J150107.16 + 284539.2	WISEA J150107.08 + 284539.7	4443809	−999	−999	733373	False	True
3008	142.246120	28.75796	1228	1459	1459	PGC 1845056	SDSS J092859.06 + 284528.5	1845056	84921	410169	194058	False	True
3009	128.807646	28.75335	2052	3525	2244	UGC 04482	UGC 04482	24104	156791	647654	4482	False	True

Note. Galaxies without a corresponding ID in columns 9–12 are denoted as −999.

(This table is available in its entirety in machine-readable form.)

Table 8
Environmental Properties of Catalog Galaxies

VFID	SGX (h^{-1} Mpc)	SGY (h^{-1} Mpc)	SGZ (h^{-1} Mpc)	$n_{5,2D}$ (h^2 Mpc^{-2})	err($n_{5,2D}$) (h^2 Mpc^{-2})	$n_{5,3D}$ (h^3 Mpc^{-3})	err($n_{5,3D}$) (h^3 Mpc^{-3})	Nearest Filament	$D_{\rm Filament}$2D (h^{-1} Mpc)	$D_{\rm Filament}$3D (h^{-1} Mpc)	Filament Memb.	Group	Cluster	Pure Field
(1)	(2)	(3)	(4)	(5)	(6)	(7)	(8)	(9)	(10)	(11)	(12)	(13)	(14)	(15)
VFID3000	2.0	11.3	−3.1	1.9	0.9	0.2	0.1	Coma_Berenices	1.2	2.0	0	2	0	0
VFID3001	2.0	5.8	−3.2	0.4	0.2	0.1	0.0	Leo_Minor	1.4	1.5	1	0	0	0
VFID3002	0.3	11.6	1.7	0.9	0.4	0.2	0.1	Canes_Venatici	1.4	1.4	1	0	0	0
VFID3003	3.9	15.7	−6.3	4.5	2.0	0.5	0.2	LeoII_B	0.1	1.9	1	2	0	0
VFID3004	12.4	18.3	−17.9	0.4	0.2	0.1	0.0	LeoII_A	4.8	7.4	0	0	0	1
VFID3005	2.7	33.8	−1.8	2.7	1.2	0.7	0.3	Coma_Berenices	4.1	4.1	0	0	0	1
VFID3006	0.3	7.1	10.7	0.1	0.0	0.0	0.0	Serpens	5.5	6.8	0	1	0	0
VFID3007	−0.6	17.7	12.3	1.1	0.5	0.1	0.0	Serpens	5.2	6.4	0	0	0	1
VFID3008	4.9	11.3	−7.7	0.4	0.2	0.0	0.0	LeoII_B	0.4	2.5	0	0	0	1
VFID3009	15.6	22.4	−22.4	0.1	0.0	0.0	0.0	LeoII_A	10.3	14.2	0	1	0	0

(This table is available in its entirety in machine-readable form.)

1. Column (1)—VFID, galaxy unique serial number;
2. Columns (2)–(4)—SG X, Y, and Z coordinates, computed as described in Section 3.1;
3. Columns (5) and (6)—local surface number density and 1σ Poisson uncertainty computed as described in Section 4.2;
4. Columns (7) and (8)—local volume number density and 1σ Poisson uncertainty computed as described in Section 4.2;
5. Column (9)—Name of the nearest filament;
6. Column (10)—2D distance of the galaxy from the nearest filament;
7. Column (11)—3D distance of the galaxy from the nearest filament;
8. Column (12)—filament member flag, where 1 indicates that the galaxy is a filament member, i.e., within $2h^{-1}$ Mpc from the nearest filament spine.
9. Column (13)—group membership flag, according to the group definition by Kourkchi & Tully (2017): 0 means the galaxy is not a member of a group, 1 means the galaxy is a member of a poor group ($2 \leqslant N < 5$), and 2 means the galaxy is a member of a rich group ($N \geqslant 5$), see text for details;
10. Column (14)—cluster membership flag as described in Section 3.2, where 1 indicates that the galaxy is a cluster member;
11. Column (15)—pure field galaxy flag, obtained as described in Section 4, where 1 indicates that the galaxy is a pure field galaxy.

ORCID iDs

Gianluca Castignani https://orcid.org/0000-0001-6831-0687
Benedetta Vulcani https://orcid.org/0000-0003-0980-1499
Rose A. Finn https://orcid.org/0000-0001-8518-4862
Francoise Combes https://orcid.org/0000-0003-2658-7893
Pascale Jablonka https://orcid.org/0000-0002-9655-1063
Gregory Rudnick https://orcid.org/0000-0001-5851-1856
Dennis Zaritsky https://orcid.org/0000-0002-5177-727X
Kelly Whalen https://orcid.org/0000-0002-8571-9801
Gabriella De Lucia https://orcid.org/0000-0002-6220-9104
Vandana Desai https://orcid.org/0000-0002-1340-0543
John Moustakas https://orcid.org/0000-0002-2733-4559

References

Abazajian, K. 2008, ApJS, 182, 543
Aguerri, J. A., Méndez-Abreu, J., & Corsini, E. M. 2009, A&A, 495, 491
Alpaslan, M., Robotham, A. S., Obreschkow, D., et al. 2014, MNRAS, 440, L106
Aragon-Calvo, M. A., Platen, E., van de Weygaert, R., & Szalay, A. S. 2008, ApJ, 723, 364
Astropy Collaboration, Robitaille, T. P., Tollerud, E. J., et al. 2013, A&A, 558, A33
Astropy Collaboration, Price-Whelan, A. M., Sipőcz, B. M., et al. 2018, AJ, 156, 123
Barazza, F. D., Jogee, S., & Marinova, I. 2007, ApJ, 675, 1194
Beygu, B., Peletier, R. F., van der Hulst, J. M., et al. 2017, MNRAS, 464, 666
Biviano, A., Fadda, D., Durret, F., Edwards, L. O. V., & Marleau, F. 2011, A&A, 532, A77
Blanton, M. R., Kazin, E., Muna, D., Weaver, B. A., & Price-Whelan, A. 2011, AJ, 142, 31
Blanton, M. R., Lupton, R. H., Schlegel, D. J., et al. 2005, ApJ, 631, 208
Blue Bird, J., Davis, J., Luber, N., et al. 2020, MNRAS, 492, 153
Bond, J. R., Kofman, L., & Pogosyan, D. 1995, Natur, 380, 603
Boselli, A., Cortese, L., & Boquien, M. 2014a, A&A, 564, 65
Boselli, A., Cortese, L., Boquien, M., et al. 2014b, A&A, 564, 67
Boselli, A., Cortese, L., Boquien, M., et al. 2014c, A&A, 564, 66
Boselli, A., Voyer, E., Boissier, S., et al. 2014d, A&A, 570, 69
Brouwer, M. M., Cacciato, M., Dvornik, A., et al. 2016, MNRAS, 462, 4451
Castignani, G., Combes, F., Jablonka, P., et al. 2022, A&A, 657, A9
Cautun, M., van de Weygaert, R., Jones, B. J. T., & Frenk, C. S. 2014, MNRAS, 441, 2923
Chen, Y. C., Ho, S., Brinkmann, J., et al. 2016, MNRAS, 461, 3896
Chen, Y. C., Ho, S., Tenneti, A., et al. 2015, MNRAS, 454, 3341
Chen, Y.-M., Shi, Y., Wild, V., et al. 2019, MNRAS, 489, 5709
Chung, A., Van Gorkom, J. H., Kenney, J. D., Crowl, H., & Vollmer, B. 2009, AJ, 138, 1741
Codis, S., Jindal, A., Chisari, N. E., et al. 2018, MNRAS, 481, 4753
Courtois, H. M., Pomarède, D., Tully, R. B., Hoffman, Y., & Courtois, D. 2013, AJ, 146, 69
Cowan, N. B., & Ivezić, Z. 2008, ApJ, 674, L13
Darvish, B., Mobasher, B., Sobral, D., et al. 2015, ApJ, 814, 84
Darvish, B., Sobral, D., Mobasher, B., et al. 2014, ApJ, 796, 51
Davies, J. I., Wilson, C. D., Auld, R., et al. 2010, MNRAS, 409, 102
Dey, A., Schlegel, D. J., Lang, D., et al. 2019, AJ, 157, 168
Dressler, A. 1980, ApJ, 236, 351
Durbala, A., Finn, R. A., Odekon, M. C., et al. 2020, AJ, 160, 271
Eardley, E., Peacock, J. A., McNaught-Roberts, T., et al. 2015, MNRAS, 448, 3665
Eskridge, P. B., Frogel, J. A., Pogge, R. W., et al. 1999, AJ, 119, 536
Fadda, D., Biviano, A., Marleau, F. R., Storrie-Lombardi, L. J., & Durret, F. 2008, ApJL, 672, L9
Ferrarese, L., Côté, P., Cuillandre, J. C., et al. 2012, ApJS, 200, 4
Fouqué, P., Solanes, J. M., Sanchis, T., & Balkowski, C. 2001, A&A, 375, 770
Fraser-McKelvie, A., Merrifield, M., Aragón-Salamanca, A., et al. 2020, MNRAS, 499, 1116
Galárraga-Espinosa, D., Aghanim, N., Langer, M., Gouin, C., & Malavasi, N. 2020, A&A, 641, 173
Geach, J. E., Ellis, R. S., Smail, I., Rawle, T. D., & Moran, S. M. 2011, MNRAS, 413, 177
Giovanelli, R., Haynes, M. P., Kent, B. R., et al. 2005, AJ, 130, 2598
Goh, T., Primack, J., Lee, C. T., et al. 2018, MNRAS, 483, 2101
Guo, H., Zheng, Z., Zehavi, I., et al. 2014, MNRAS, 441, 2398
Haynes, M. P., Giovanelli, R., Kent, B. R., et al. 2018, ApJ, 861, 49
Hirv, A., Pelt, J., Saar, E., et al. 2017, A&A, 599, A31
Hoyle, F., Rojas, R. R., Vogeley, M. S., & Brinkmann, J. 2005, ApJ, 620, 618
Huchra, J. P., MacRi, L. M., Masters, K. L., et al. 2012, ApJS, 199, 26
Hunter, J. D. 2007, CSE, 9, 90
Jaffé, Y. L., Smith, R., Candlish, G. N., et al. 2015, MNRAS, 448, 1715
James, P. A., & Percival, S. M. 2016, MNRAS, 457, 917
Jasche, J., Kitaura, F. S., Li, C., & Enßlin, T. A. 2010, MNRAS, 409, 355
Joeveer, M., Einasto, J., & Tago, E. 1978, MNRAS, 185, 357
Karachentsev, I. D., & Nasonova, O. G. 2010, MNRAS, 405, 1075
Kim, S., Rey, S.-C., Bureau, M., et al. 2016, ApJ, 833, 207
Kim, S., Rey, S.-C., Jerjen, H., et al. 2014, ApJS, 215, 22
Kleiner, D., Pimbblet, K. A., Heath Jones, D., Koribalski, B. S., & Serra, P. 2017, MNRAS, 466, 4692
Ko, Y., Hwang, H. S., Lee, M. G., et al. 2017, ApJ, 835, 212
Kourkchi, E., & Tully, R. B. 2017, ApJ, 843, 16
Koyama, Y., Kodama, T., Nakata, F., Shimasaku, K., & Okamura, S. 2011, ApJ, 734, 66
Koyama, Y., Kodama, T., Tadaki, K.-I., et al. 2014, ApJ, 789, 18
Kraljic, K., Arnouts, S., Pichon, C., et al. 2018, MNRAS, 474, 547
Kraljic, K., Duckworth, C., Tojeiro, R., et al. 2021, MNRAS, 504, 4626
Kraljic, K., Pichon, C., Dubois, Y., et al. 2019, MNRAS, 483, 3227
Kreckel, K., Platen, E., Aragón-Calvo, M. A., et al. 2011, AJ, 141, 4
Kuchner, U., Aragón-Salamanca, A., Pearce, F. R., et al. 2020, MNRAS, 494, 5473
Kuchner, U., Aragón-Salamanca, A., Rost, A., et al. 2021, MNRAS, 503, 2065
Kuutma, T., Tamm, A., & Tempel, E. 2017, A&A, 600, L6
Laigle, C., Pichon, C., Arnouts, S., et al. 2018, MNRAS, 474, 5437
Lang, D., Hogg, D. W., & Mykytyn, D. 2016, The Tractor: Probabilistic astronomical source detection and measurement, Astrophysics Source Code Library, ascl:1604.008
Lee, Y., Kim, S., Rey, S.-C., & Chung, J. 2021, ApJ, 906, 68
Leroy, A. K., Sandstrom, K. M., Lang, D., et al. 2019, ApJS, 244, 24
Libeskind, N. I., Carlesi, E., Grand, R. J., et al. 2020, MNRAS, 498, 2968
Libeskind, N. I., van de Weygaert, R., Cautun, M., et al. 2018, MNRAS, 473, 1195

Mahajan, S., Raychaudhury, S., & Pimbblet, K. A. 2012, MNRAS, 427, 1252
Mahajan, S., Singh, A., & Shobhana, D. 2018, MNRAS, 478, 4336
Makarov, D., Prugniel, P., Terekhova, N., Courtois, H., & Vauglin, I. 2014, A&A, 570, 13
Malavasi, N., Aghanim, N., Douspis, M., Tanimura, H., & Bonjean, V. 2020a, A&A, 642, A19
Malavasi, N., Aghanim, N., Tanimura, H., Bonjean, V., & Douspis, M. 2020b, A&A, 634, A30
Malavasi, N., Arnouts, S., Vibert, D., et al. 2017, MNRAS, 465, 3817
Marinova, I., & Jogee, S. 2007, ApJ, 659, 1176
McLaughlin, D. E. 1999, ApJ, 512, L9
Mei, S., Blakeslee, J., Cote, P., et al. 2007, ApJ, 655, 144
Mould, J. R., Huchra, J. P., Freedman, W. L., et al. 2000, ApJ, 529, 786
Muldrew, S. I., Croton, D. J., Skibba, R. A., et al. 2012, MNRAS, 419, 2670
Newnham, L., Hess, K. M., Masters, K. L., et al. 2020, MNRAS, 492, 4697
Odekon, M. C., Hallenbeck, G., Haynes, M. P., et al. 2018, ApJ, 852, 142
Pintos-Castro, I., Sánchez-Portal, M., Cepa, J., et al. 2013, A&A, 558, A100
Porter, S. C., & Raychaudhury, S. 2006, MNRAS, 375, 1409
Porter, S. C., Raychaudhury, S., Pimbblet, K. A., & Drinkwater, M. J. 2008, MNRAS, 388, 1152
Postman, M., & Geller, M. J. 1984, ApJ, 281, 95
Reese, A. S., Williams, T. B., Sellwood, J. A., Barnes, E. I., & Powell, B. A. 2007, AJ, 133, 2846
Riess, A. G., Casertano, S., Yuan, W., Macri, L. M., & Scolnic, D. 2019, ApJ, 876, 85
Rojas, R. R., Vogeley, M. S., Hoyle, F., & Brinkmann, J. 2004, ApJ, 617, 50
Rost, A., Kuchner, U., Welker, C., et al. 2021, MNRAS, 502, 714
Santos, J. S., Altieri, B., Tanaka, M., et al. 2014, MNRAS, 438, 2565
Sobral, D., Best, P. N., Smail, I., et al. 2011, MNRAS, 411, 675
Steer, I., Madore, B. F., Mazzarella, J. M., et al. 2017, AJ, 153, 37
Taylor, M. B. 2005, in ASP Conf. Ser., 347, Astronomical Data Analysis Software and Systems XIV, ed. P. Shopbell, M. Britton, & R. Ebert (San Francisco, CA: ASP), 29
Tempel, E., & Libeskind, N. I. 2013a, ApJL, 775, L42
Tempel, E., & Libeskind, N. I. 2013b, ApJL, 775, 42
Tempel, E., Stoica, R. S., Mart\'\inez, V. J., et al. 2014, MNRAS, 438, 3465
Tempel, E., Stoica, R. S., & Saar, E. 2013, MNRAS, 428, 1827
Tifft, W. G., & Gregory, S. A. 1976, ApJ, 205, 696
Tully, R. B. 1982, ApJ, 257, 389
Tully, R. B., Courtois, H., Hoffman, Y., & Pomarède, D. 2014, Natur, 513, 71
Tully, R. B., Courtois, H. M., Dolphin, A. E., et al. 2013, AJ, 146, 86
Tully, R. B., Courtois, H. M., & Sorce, J. G. 2016, AJ, 152, 50
Tully, R. B., Rizzi, L., Shaya, E. J., et al. 2009, AJ, 138, 323
Tully, R. B., Shaya, E. J., Karachentsev, I. D., et al. 2008, ApJ, 676, 184
Vulcani, B., Poggianti, B. M., Moretti, A., et al. 2019, MNRAS, 487, 2278
Welker, C., Bland-Hawthorn, J., van De Sande, J., et al. 2020, MNRAS, 491, 2864
Yan, H., Fan, Z., & White, S. D. 2013, MNRAS, 430, 3432
Zhang, Y., Yang, X., Wang, H., et al. 2013, ApJ, 779, 160